SANDIA REPORT

SAND2005-7954
Unlimited Release
Printed January 2006

Friction of Different Monolayer Lubricants in MEMs Interfaces

Alex D. Corwin, Mark D. Street, Robert W. Carpick, William R. Ashurst,
Michael J. Starr and Maarten P. de Boer

Prepared by
Sandia National Laboratories
Albuquerque, New Mexico 87185 and Livermore, California 94550

Sandia National Laboratories

Issued by Sandia National Laboratories, operated for the United States Department of Energy by Sandia Corporation.

Available to DOE and DOE contractors from
U.S. Department of Energy
Office of Scientific and Technical Information
P.O. Box 62
Oak Ridge, TN 37831

Telephone: (865) 576-8401
Facsimile: (865) 576-5728
E-Mail: reports@adonis.osti.gov
Online ordering: http://www.osti.gov/bridge

Available to the public from
U.S. Department of Commerce
National Technical Information Service
5285 Port Royal Rd.
Springfield, VA 22161

Telephone: (800) 553-6847
Facsimile: (703) 605-6900
E-Mail: orders@ntis.fedworld.gov
Online order: http://www.ntis.gov/help/ordermethods.asp?loc=7-4-0#online

SAND2005-7954
Unlimited Release
Printed January 2006

Friction of Different Monolayer Lubricants in MEMs Interfaces

Alex D. Corwin,
Mems Technology S&T; Michael J. Starr,;
Structural Dynamics Research Department
and Maarten P. de Boer,
MEMS Devices & Rel Phys I;
Sandia National Laboratories,
Albuquerque, NM 87185

Mark D. Street and Robert W. Carpick
University of Wisconsin,
Madison, WI 53706

William R. Ashurst
Auburn University,
Auburn, AL 36849

ABSTRACT

This report details results from our last year of work (FY2005) on friction in MEMS as funded by the Campaign 6 program for the Microscale Friction project. We have applied different monolayers to a sensitive MEMS friction tester called the nanotractor. The nanotractor is also a useful actuator that can travel ±100 μm in 40 nm steps, and is being considered for several MEMS applications. With this tester, we can find static and dynamic coefficients of friction. We can also quantify deviations from Amontons' and Coulomb's friction laws. Because of the huge surface-to-volume ratio at the microscale, surface properties such as adhesion and friction can dominate device performance, and therefore such deviations are important to quantify and understand. We find that static and dynamic friction depend on the monolayer lubricant applied. The friction data can be modeled with a non-zero adhesion force, which represents a deviation from Amontons' Law. Further, we show preliminary data indicating that the adhesion force depends not only on the monolayer, but also on the normal load applied. Finally, we also observe slip deflections before the transition from static to dynamic friction, and find that they depend on the monolayer.

ACKNOWLEDGMENTS

We thank Frank Delrio for carrying out some of the AFM measurements looking for particles.

CONTENTS

FIGURES

I. INTRODUCTION

The "laws" of friction were derived from experimentation [1] and are commonly used today by engineers to calculate the response of interfaces subject to simultaneous compressive and shear loading. The first two laws are attributed to Amontons [2] (who used pork fat as a boundary lubricant to get consistent results) and state (1) that friction force is proportional to load and (2) that friction force is independent of the apparent contact area. A third law is attributed to Coulomb [3] and states (3) that dynamic friction is lower than static friction and independent of the sliding velocity. These "laws" describe the first order behavior interfaces subjected to mechanical loads, but deviations have long been recognized. For example, it has been known since the 18th century that adhesion causes a deviation from the first law [3,4]. Recently, friction under tensile load has been directly observed in nanometer-sized single asperities [5] and in a surface-micromachined structure [6]. Also, before the transition from static to dynamic friction, slip displacements up to several microns are commonly measured for macroscopic sliders [7,8]. This slip characteristic can in turn be responsible for the transition from stick-slip to steady-state sliding [9]. Without this energy dissipation mechanism, undamped harmonic oscillations would persist in the slider, independent of velocity [10]. Experimental observations such as the logarithmic increase of static friction with time [3,11,12] and logarithmic decrease of dynamic friction with velocity [13] have been incorporated into empirical rate and state models of the interface [14]. Such models, which incorporate the notion of a memory effect at the contacting asperities, shed light on such diverse phenomena as earthquake nucleation [15], dynamic fracture [16] and granular slip [17].

Surface micromachining is a technology in which micrometer-scale mechanical structures are formed by lithographic methods [18]. Applications such as accelerometers [19] and pressure sensors [20] are very successful in part because contact is not allowed between structures. At present, components that allow contact between structures such as gears, hinges and guides operate successfully, but their durability can be limited by tribological failure [21]. Indeed, if the laws of friction and wear were well known at the microscale, it is possible that many more applications could be reliably engineered.

In previous work, we inferred that adhesion [6] needs to be taken into account and that small-scale slip [22,23] strongly affects the operation of surface-micromachined actuator that relies on friction to develop force [24]. Our aim here is to quantify deviations from the classical "laws" of friction for different monolayer lubricants that are applied to the surfaces. First, we wish to examine Amontons' First Law. We find that adhesion force depends on the lubricant and further that it is not constant when normal load is varied over a wide range. Second, we wish to quantitatively examine where dynamic friction is smaller than static friction. Our evidence indicates that the Third Law holds for one lubricant. However, for another lubricant that we study, static and dynamic friction are indistinguishable. Third, we develop a nanometer-scale metrology and examine directly whether slip prior to the transition from static to dynamic friction occurs. We find that it does and further observe that its detailed behavior depends very strongly on the lubricant. In particular, an eight-carbon perfluorinated molecular lubricant exhibits stable pre-sliding tangential deflections (PSTD) up to hundreds of nanometers in length, while an eighteen-carbon chain hydrocarbon molecular lubricant exhibits creep-like behavior of many microns in length. We suggest that local differences in contacting asperity distributions are responsible for the former characteristic while an activated process is likely the governing mechanism for the latter characteristic. We also compare our results to the rate and state framework and conclude that the short chain lubricant may fall into that framework while the long chain lubricant apparently does not.

II. SURFACE-MICROMACHINED FRICTION TESTER

In MEMS, friction occurs at the interface formed when two structures, fabricated independently, are brought into contact. The fabrication technology used to build the structures is known as polycrystalline silicon (polysilicon) surface micromachining. Using a process of repeated deposition, lithography and etching steps, the technology enables five independent structural levels to be formed [18]. The thickness of the structural levels is typically 2.25 μm, while the lines and spaces between structures on the same level is as small as 1 μm. The vertical gap between different structural levels, which is formed by deposited "sacrificial" oxide layers, is typically 2 μm. Upper sacrificial layers are planarized by a chemical mechanical polishing process to ensure that each new level of polysilicon is formed on a planar surface. All sacrificial layers are removed at the end of the process to render the structures free-standing.

To make our measurements we have developed a surface micromachined linear actuator, called a nanotractor[1], that uses friction to achieve high performance characteristics [24]. The nanotractor is being considered for several applications at Sandia National Laboratories including the discriminating microswitch and TOPAS, and also by a company that Sandia is working with. It moves both forwards and backwards in ~50 nanometer steps over a travel distance of ±100 μm and can develop a force of up to 2.5 milliNewtons. (The comb drive actuator, which is commonly used in surface micromachining [25,26], can move up to ±20 μm and delivers a smaller force of ~20 microNewtons). The nanotractor can be operated at speeds up to ~ 3 mm/sec. It consists of two frictional clamps spanned by an actuation plate, as seen in Figure 1(a). Through an appropriately-phased sequence of clamping voltages, we can walk the nanotractor in 50 nm steps against the tangential force of a linear suspension spring. The clamping force, acting normal to the surface, is applied electrostatically and is borne mechanically by equipotential rubbing counterfaces, as seen in Fig. 1(b). The upper counterface is called the friction foot. Knowing the geometry of the parallel plate clamping electrodes and the clamping voltage, we can determine the normal clamping force F_c. The clamping force resolution is 0.01 μN and the range is from 0 to 10 milliNewton (mN) in these experiments.

Suspension springs, as shown in Figure 1(a), are linear due to their fixed-guided geometries. Their in-plane spring constants k_x are on the order of 1 N/m, depending on the linewidth of the spring, as can be verified through a resonant frequency measurement. These springs serve both to center the nanotractor and to present an in-plane restoring force to the nanotractor. They have an out-of-plane spring constant k_z also on the order of 1 N/m and again depending on the linewidth. Before initial operation, the clamps are suspended a distance z_{off} above the surface, with z_{off} depending on the design. The tensile force $k_z\, z_{off}$ needs to be taken into account to accurately evaluate the total applied normal load.

---

[1] The actuator was originally called an inchworm. However, Inchworm^{R} is a registered trademark of Burleigh Instruments in the field of electromechanical actuators, and refers to a piezoelectric-based mechanism.

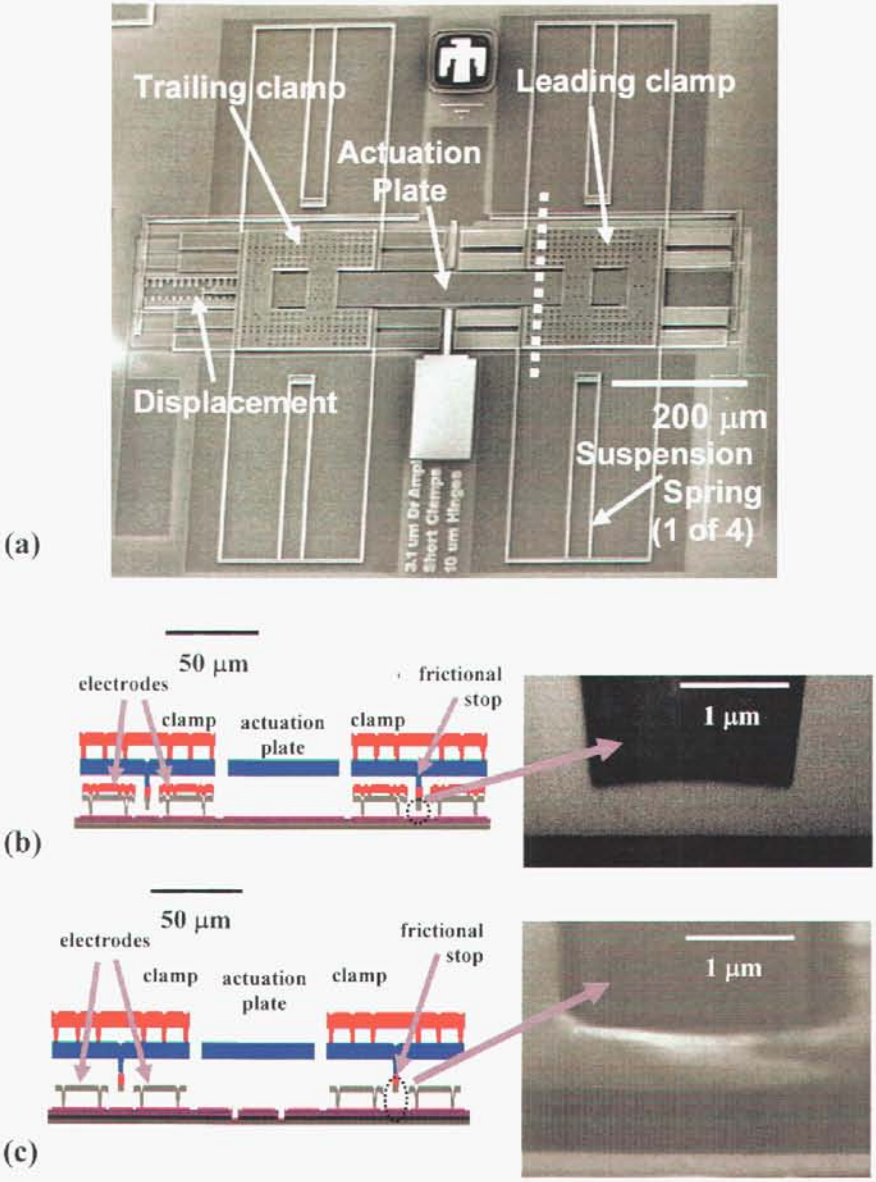

Figure 1 a) SEM image of the nanotractor device. b) Left side - A schematic cross-section through the dotted line indicated part a (looking down the length of the device). A given clamp is fabricated on each side of the plate to ensure electromechanical stability. The gap between the friction stop and its underlying counterface is smaller than the gap between the clamp electrodes and the clamp. Thus, the upper frictional counterface also serves as a mechanical stop when the clamp is energized. Only 2 volts are required to bring the friction stops into contact with the substrate, but up to 200 volts can be applied, allowing a μN to mN normal force range. Right side – close up SEM of foot. The lower dark area is the lower polysilicon counterface, while the upper dark area is the upper counterface. (Lot 247 design, before the sacrificial oxide is removed) c) Same as (b), but Lot 415 design. The foot is now perfectly flat.

The polysilicon in surface micromachining is deposited amorphously by low-pressure chemical vapor deposition and then annealed at high temperature to relieve residual stresses. The resulting grain size is ~1 um, while the surface roughness is several nanometers root mean square (rms). Using a curve-fitting routine, the typical radius of curvature of asperities is $R \approx 100$ nm. Considering the contact mechanics of rough surfaces, the contacting diameter at initial asperities is $2a \approx 10$ nm. Fig. 2(a) shows typical topography of the lower counterface. The nanotractor friction feet were intentionally designed to be large (4800 μm^2) to maximize the effect of friction in the experiments, and the results are expected to give a good average for what would be measured if the nominal contact area were smaller, as is typical in MEMS devices (<100 μm^2). More details on the particular designs used here will be given in the experimental section below.

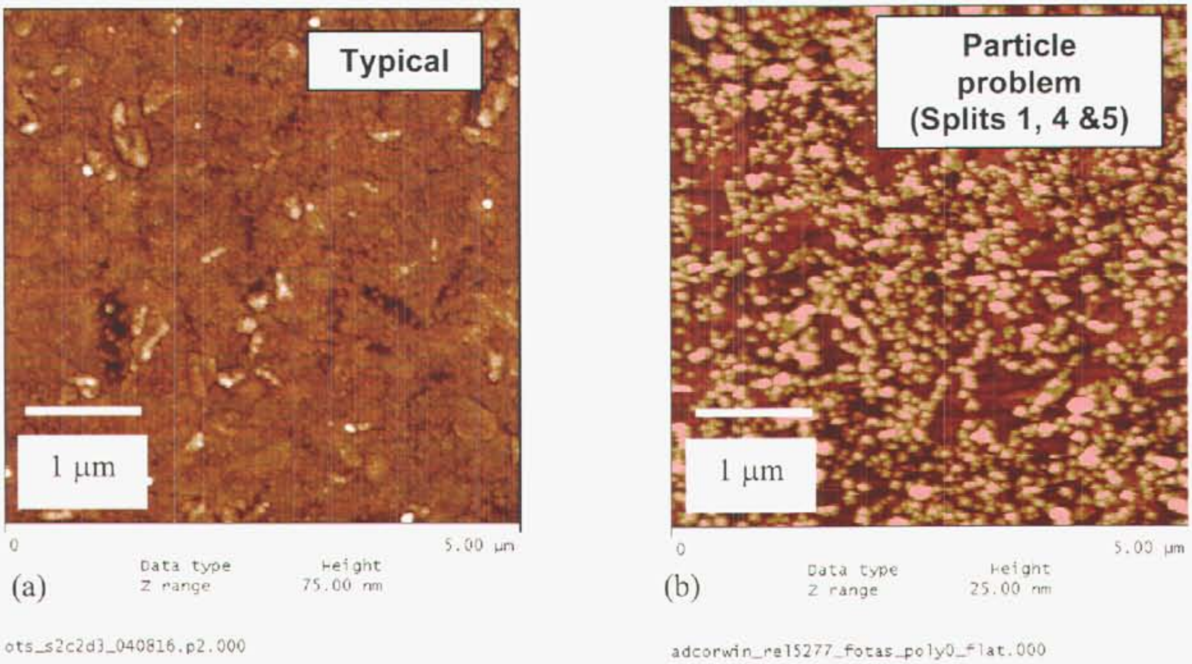

Figure 2 lower counterface showing roughness of polysilicon. (a) typical roughnness (OTS, lot 247). (b) atypical roughness showing very high particle count (FOTAS, Lot 415)

As described to this point, the nanotractor is a stepper motor. In the following section, we describe how the monolayer lubricant can be varied and discuss in some detail what is known about the monolayer structure in each case. In sections thereafter, we describe how the nanotractor is employed to make static, adhesion, dynamic and pre-sliding (slip) tests. We then present test results and discussion.

III. MONOLAYER LUBRICANTS

At the end of fabrication process, the sacrificial oxide is dissolved in 1:1 HF:HCl mixture, which etches the mechanical polysilicon structures at a negligible rate. Structures are then rinsed in water. If they are dried in air, capillary action will bring these highly compliant structures into contact with the substrate and cause them to permanently adhere [27,28]. Free-standing structures can be made in several ways. These methods include critical point drying and the application of monolayer lubricants. Because monolayer chemistry and structure strongly affects friction characteristics, we applied three different monolayers.

For the first monolayer, we used critical point drying using super critical carbon-dioxide as the working fluid [29] to first obtain freestanding structures. The surfaces were then cleaned in an oxygen plasma to remove any airborne contaminants and to terminate the surface with hydroxyl groups. They were then vacuum-transferred to a vapor deposition chamber, where a tridecafluoro-1,1,2,2-tetrahydrodecyltris(dimethylamino)silane ($CF_3C_5F_{10}C_2H_4Si(N(CH_3)_2)_3$,FOTAS) [30] monolayer film was applied. The FOTAS has a tri-amino head group that promotes chemical bonding to the silanol surface via a nucleophilic reaction, and a perfluorinated tail group to minimize surface energy. The advantage of the vapor-deposition technique lies in its manufacturability [31], and FOTAS is the standard coating applied in the SUMMiT V^{TM} process.

For the second monolayer, we applied an octadecyltrichlorosilane ($CH_3(CH_2)_{17}SiCl_3$, OTS) monolayer coating [32]. In this case, processing is by a solvent-based route. From water, the structures are oxidized in 70 °C hydrogen peroxide solution to again obtain surface hydroxyl groups. We then transferred them from water through a series of miscible solvents to 1 mM OTS in hexane at room temperature, where the lubricant deposition occurs. The structures are then transferred in reverse sequence through the solvents back to water. Because the contact angle of water with the OTS surface is ~110°, capillary forces are repulsive and the structures are not only freestanding but also lubricated when directly removed from water. The third monolayer we applied was octadecene ($C_{16}H_{33}CH{=}CH_2$), again applied from solution [33].

We also shall report on some samples where no monolayer was applied. These samples received critical point drying. In some cases they also were cleaned by oxygen plasma to reduce airborne contaminants as well as contaminants introduced by the critical point drying process.

There are several reasons for studying monolayers other than the standard monolayer used in the SUMMiT^{TM} process, FOTAS. First, FOTAS was chosen because as a vapor coating, it is considered to be more manufacturable than the liquid-based coatings. To obtain a broad picture of the performance tradeoffs, it is important to quantify other monolayers as well. Second, by comparing the numbers we measure and combining this with our knowledge of film structure, we arrive at a better understanding of the structure/property relationships of the monolayers. Third, unknown effects may be discovered in the other monolayers. It is important to determine if they also exist in a subtle way for FOTAS. An example of this is the creep-like stress relaxation we measure for OTS, as reported in Section V.5. Does FOTAS also show this creep at a temperature higher than room temperature, as it may experience in the field?

Based on literature studies, we now qualitatively discuss the structure of monolayers, beginning with a well-studied system. Alkanethiols ($CH_3(CH_2)_nSH$) on (111) gold have been much studied [34]. For normal alkane chains, the van der Waals binding energy is ~7 kJ/mol [35]. Thus for an eighteen-carbon chain (n=18), the binding energy is ~130 kJ/mol. A typical covalent bond energy is from 100-300 kJ/mol. For longer chain hydrocarbons, it is expected that the van der Waals energy will strongly affect the degree of molecular packing. For alkanethiols on (111) gold, the lattice spacing is larger than the alkane diameter. Hence, chains in which $n \geq 16$ tilt 30° to minimize energy [34]. As the chains shorten, the tilt angle gradually increases to ~34° for n=10. This is thought to be due to the increasing influence of the substrate interaction. For $n \geq 10$, however, there is long-range order in the chain structure, and the films are truly self-assembled monolayers (SAMs). For $n \leq 7$, it is not clear if the packing density of the monolayer decreases or if the tilt increases even more [36]. In either case, it is likely that the chains have higher gauche defect concentrations and weaker interactions with each other. Essentially, a loss of conformational entropy is not overcome by reducing van der Waals energy in these short chain molecules, and the structure is thought to be more disordered.

The situation for alkylsilanes (e.g., OTS) deposited on hydroxyl-terminated amorphous SiO_2 is more complicated. The head group transforms from $SiCl_3$ to $Si(OH)_3$ in solution and then initially physisorbs to a thin water layer via a hydrogen bonding interaction (SiOH-SiOH). At room temperature, liquid-condensed (LC) and liquid-expanded (LE) phases co-exist [37]. The LC phase develops by island growth, as the chains stand up and presumably exhibit local ordering. In the LE phase the structure is surely more disordered and evolves as the deposition proceeds. Eventually, film growth ends as the thickness of the LE areas (~90% of the nominal area at room temperature) become indistinguishable from the LC islands (~10% of the area). Deposition times are on the order of 15 minutes. Within hours after deposition (in air), substrate grafting via a condensation reaction ensues, with a resulting chemisorbed Si-O-Si bond. Other OH groups associated with the head group are available to bond with each other, and so can potentially form a cross-linked in-plane network [38]. However, the head-group spacing will be smaller than the chain radius [39]. In turn, no long range order persists even in the alklysilanes [38]. For example, using grazing-incidence X-ray diffraction (GIXD), the in-plane correlation length for OTS is 45 Å [40]. The LC areas do remain distinguishable from the LE areas in atomic force microscope images, especially in friction force images. An example will be shown below. GIXD measurements also show a molecular areal density of $4.95/nm^2$ for OTS [40]. The theoretical density of alkyl chains is $5.43/nm^2$ [34]. For comparison, alkanethiols are limited by the interatomic spacing of (111) Au and their areal density of $4.63/nm^2$ [34].

We will show that the OTS layers are monolayers in the present experiments. However, the process window for obtaining monolayers is small and it is well known that OTS molecules can also polymerize in the bulk solvent, with the result that 20-100 nm diameter agglomerates deposit on the surface [33,41]. This leads to incomplete coverage and unpredictable adhesion results [42]. To address this process variability issue, vapor phase lubricants, which in general can only react at the surface, have been developed. Initially, these were also trichlorosilane based [31]. However, water must be added to the reaction to help activate the sluggish kinetics of the $CF_3(CF_2)_5(CH_2)_2SiCl_3$ (labeled FOTS). Therefore, the more reactive tris(dimethylamino) ($Si(NCH_3)_3$) (FOTAS) architecture has more recently been developed to enhance the reaction kinetics [30], resulting in more reproducible and faster processing.

The structural differences between FOTS [31] and FOTAS [30] are expected to be small. Indeed, for each the water contact angle is ~114°. However, the structure of these films is expected to be substantially different from OTS for several reasons. First, the tail groups are shorter (n=8 versus n=18). Second, the van der Waals diameter of the fluorocarbon chain is 20% larger than that of the hydrocarbon chain. For either precursor, some degree of head group polymerization will occur over time, so again this imposed strain will further disorder the even larger fluorocarbon groups. Very likely, the FOTAS film exhibits no local ordering and can be thought of as more tilted (i.e., flatter) and more entangled than the alkanethiols of equivalent chain length. Hence, we expect that FOTAS will be much more disordered than OTS. Although the vapor phase lubricants are reproducibly applied, only short chain molecules can be used. Long chain molecules require higher temperature to obtain sufficient vapor pressure, but decompose before reasonable deposition rates are achieved.

The octadecene molecule has been developed to address several issues MEMS [33]. It is deposited in liquid, so an 18-carbon chain can be used. This approach abandons the chlorosilane chemistry and adopts a free radical reaction of a primary alkene and therefore the probability of competing reactions in the bulk solvent is greatly reduced. A silicon surface terminated by Si-H groups is essential to the process. The solution is heated to generate free radicals, and a direct Si-C bond is formed between the surface and the molecule as verified by X-ray photoelectron spectroscopy (XPS) [33]. The contact angle of octadecene with water is ~104°, while it is ~110° for OTS. Similarly, the contact angle of octadecene with hexadecane is 35° while it is 38°. Although more direct investigation of the monolayer would certainly be useful, it is thought that the octadecene monolayer may be less dense than OTS. This may be because the deposition occurs at higher temperature, where disorder due to configurational entropy, is expected to be greater.

For reference in this report, we shall also describe results on nominally uncoated surfaces. These are prepared by critical point drying (CPD). Although the contaminants associated with CPD have not been identified, it is known that the contact angle of water with the surface rises from ~30° to ~70° after the CPD process. This can be lowered to near 0° after an oxygen plasma clean. The DC powered- plasma was at 800 V and 20 mA (16 Watts), for 5 minutes in O_2. Data for both of these types of samples will be given.

IV. TEST PROCEDURES AND EXPERIMENTAL DESIGN

In this section we describe how the static, dynamic and pre-sliding tangential deflection data are measured and interpreted. We then describe the experimental design in terms of the two nanotractor designs and the different monolayer coatings.

IV.1 STATIC FRICTION TEST

To carry out a static friction measurement, we first walk the nanotractor out against a load spring to a large distance, e.g., $x_0 = 40\ \mu\text{m}$ as in Fig. 3(a). Then, the leading clamp is fixed in place with a large voltage (i.e., large normal force) while the trailing clamp and plate are released as in Fig. 3(b). We then step down the voltage (force) in the leading clamp while recording the position of the nanotractor as shown in Figure 3(c). As long as the static friction force at the clamp interface, F_s, is large enough to balance the tangential force of the load spring, we expect the nanotractor to remain fixed in place. When F_s drops just below the tangential force, as in Fig. 3(d), we expect the nanotractor to slide some jump distance $\Delta = x_0 - x$. (The magnitude of Δ depends on the difference between the static and dynamic coefficients of friction, inertia and air damping).

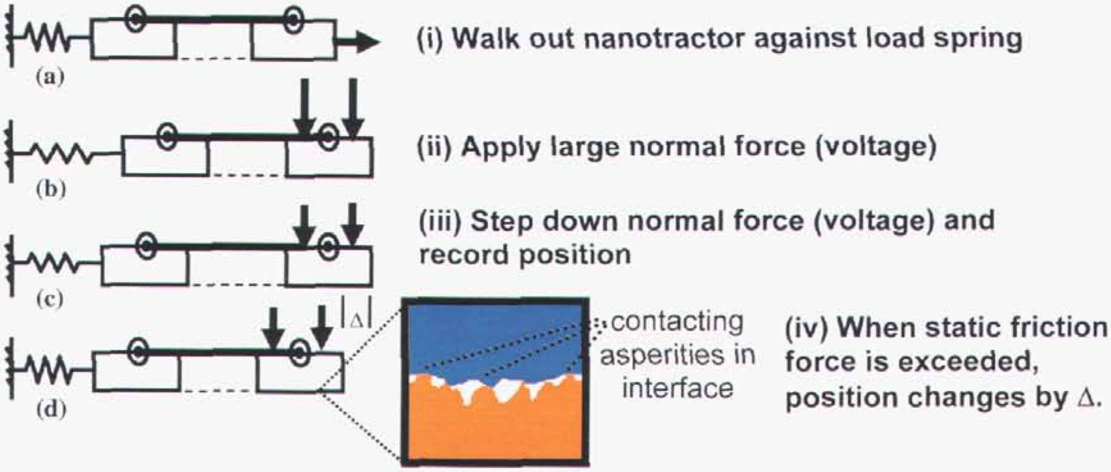

Figure 3 Schematic representation of a friction test.

The total normal force F_N includes an out-of-plane restoring force term from the tangential load spring ($k_z z_{off}$), and a gravitational mass term (mg), according to

$$F_N = F_c - k_z z_{off} + mg . \tag{1}$$

Friction is measured at zero applied load (F_N=0) due to an attractive adhesive force between the surfaces, F_A. Following Coulomb [3], we write Amontons' first law as

$$F_s = \mu_s \left(F_c + mg - k_z z_{off} \right) + \mu_s F_A , \tag{2}$$

where μ_s is the static coefficient of friction. By a best fit to the data over all jumps, we can determine both μ_s and F_A.

IV.2 NANOMETER-SCALE SLIP MEASUREMENTS

To directly observe slip before the transition from static to dynamic friction, we have applied sub-pixel measurements while viewing a moving section of the nanotractor at high optical magnification. For optimum resolution, a reference structure fixed to the substrate is used, as seen in Fig. 4. Using pattern matching and sub-pixel interpolation, the in-plane resolution is ± 10 nm displacement over the full scale of the field of view (~80 μm). Based on the ability to determine its phase to one part in 2500, the grating structure in Fig. 4 is used to obtain ±1 nm displacement information over a range of 2.5 μm (the grating pitch).

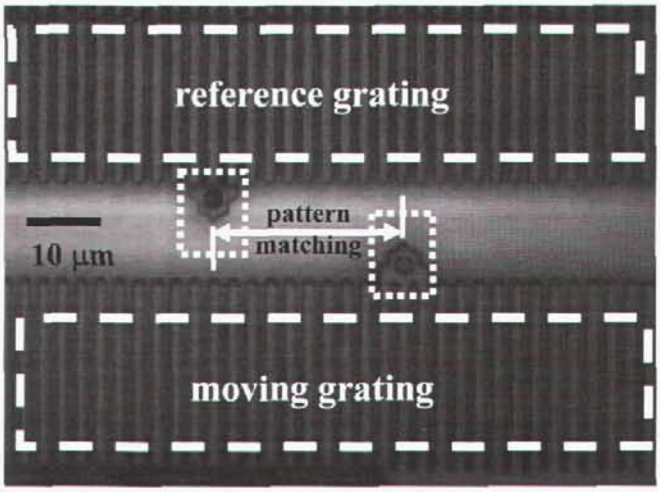

Figure 4 Structure used for high-resolution in-plane deflection information in static friction test. Pattern matching is used on the pointer structures for ± 10 nm displacement over the full scale of the field of view. Based on the ability to determine its phase to one part in 2500, the grating structure is used to obtain ±1 nm displacement information over a range of 2.5 μm (the grating pitch).

IV.3 DYNAMIC FRICTION TEST

To obtain dynamic friction information we treat the nanotractor as a one-dimensional harmonic oscillator subject to spring, inertial, air damping and frictional forces, as seen in Fig. 5. Similar to the static friction test, we first walk the nanotractor out to some large distance, e.g., x_o=60 μm. We fix it in that position with a large clamping voltage, such that the friction force is much larger than the spring force, i.e., $F_s >> k_x x$. We instantaneously reduce the clamping voltage to a value much lower value such that $F_s << k_x x$. The clamps then begin moving and the dynamic friction force F_d is now

$$F_d = \mu_d \left(F_c + mg - k_z z_{off}\right) + \mu_d F_A \qquad (3)$$

where μ_d is the dynamic coefficient of friction. By taking measurements of x-position versus time, we obtain the decay curve. From this methodology, we quantify μ_d, F_A and the air damping constant [6]. We shall refer to this as Methodology A.

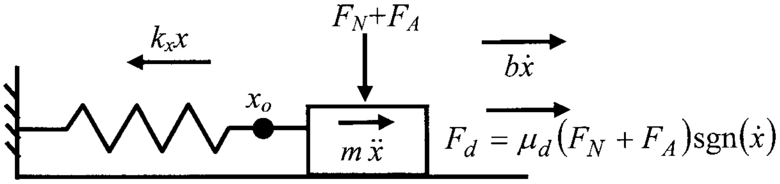

Figure 5 Schematic representation of the one-dimensional harmonic oscillator subject to dynamic friction and air damping. Initial position $x(0)=x_o$.

Although with Methodology A we obtain all the relevant parameters, it requires a large number of measurements because an electromechanical strobing technique, rather than a real-time technique, is used to obtain the data [6]. Because of the many measurements, the surface is subject to a small degree of wear. Therefore, we have revised the test to obtain data in only the first-half cycle where the equation of motion can be linearized. We shall refer to this as Methodology B.

With the convention of positive force to the left, from Fig. 4 we write the equation of motion as

$$m\ddot{x}+b\dot{x}+F_d\,\mathrm{sgn}(\dot{x})+k_x x=0, \tag{4}$$

where we have used the sign function ($\mathrm{sgn}(\dot{x})$=1 if $\dot{x}$>0, and $\mathrm{sgn}(\dot{x})$=-1 if $\dot{x}$<0), because the friction always opposes the direction of motion. In the first half cycle with $t \le \pi/\omega$, the velocity is negative as shown in Fig. 3, and therefore $\mathrm{sgn}(\dot{x})$= -1. In Eq. (4), b is the linear damping term due to air damping and $\dot{x}$ is with respect to time t. Dividing by m, we can rewrite Eq. (4) as

$$\ddot{x}+\gamma\dot{x}-\omega_0{}^2 f_d+\omega_0{}^2 x=0, \tag{5}$$

with $\omega_0{}^2=k_x/m$, $\gamma=b/m$ and $f_d=F_d/k_x$. The general solution for the first half-cycle is

$$x(t)=Ae^{-\gamma t/2}\cos(\omega t+\alpha)+f_d \tag{6}$$

with $\omega^2 = \omega_0{}^2 - \gamma^2/4$. With initial conditions of $x'(0)=0$ (zero velocity) and $x(0)=x_o$, $\alpha = \tan^{-1}(-\gamma/2\omega)$ and $A = (x_o - f_d)/\cos(\alpha)$. If we relax the normal force for some time t, the mass will travel a distance $\Delta x(t) = x_0 - x(t)$ according to

$$\Delta x(t) = x_0\left(1 - \frac{\cos(\omega t + \alpha)}{e^{\left(\frac{\gamma t}{2}\right)}\cos(\alpha)}\right) - f_d\left(1 - \frac{\cos(\omega t + \alpha)}{e^{\left(\frac{\gamma t}{2}\right)}\cos(\alpha)}\right), \tag{7a}$$

or with $\Sigma = \left(1 - \dfrac{\cos(\omega t + \alpha)}{e^{\left(\frac{\gamma t}{2}\right)}\cos(\alpha)}\right)$, (7b)

$$\Delta x(t) = \left(x_0 - \frac{(F_A + mg - k_z z)\mu_d}{k_x} - \frac{F_C \mu_d}{k_x}\right)\Sigma \tag{7c}.$$

Note that Σ in Eq. (7b) is constant if we fix $t = \Delta t$. The first term in Eq. (7c) is linear with x_0 while the last term is linear with F_C. Hence, if we systematically vary either x_0 or F_C while holding everything else constant, we expect to measure a straight line with slope and intercept values that we can relate to parameters of interest.

To obtain ω, we fix $t = \Delta t$ (such that Σ is constant), keep F_C=0 and vary x_0. The parameters γ and m are known from a previous measurement [6]. The measured slope of $\Delta x(t)$ versus x_0 ($slope_1$) is equal to Σ. Because α can be written in terms of ω, we can solve for ω using

$$\Sigma = slope_1 = \left(1 - \frac{\cos(\omega t + \alpha)}{e^{\left(\frac{\gamma t}{2}\right)} \cos(\alpha)}\right). \tag{8a}$$

As a first approximation, both α and $\gamma\ \Delta t$ are small and hence

$$\omega \approx \left(\frac{1}{\Delta t}\right) \cos^{-1}(1 - slope_1). \tag{8b}$$

From ω and γ we calculate ω_o and from this we obtain $k_x = m\ \omega_0^{\ 2}$ assuming a value for m. Next, in Eq. (7c), if F_C=0, then the x_o-intercept of $\Delta x(t)$ versus x_0 ($x_o - \text{int}_1$) gives

$$x_o - \text{int}_1 = (F_A + mg - k_z z_{off})(\mu_d / k_x). \tag{9}$$

This gives an equation for F_A and μ_d. If we now hold x_0 and Δt fixed and instead vary F_C, measurement of the slope of $\Delta x(t)$ versus F_C ($slope_2$) gives

$$slope_2 = -\left(\frac{\mu_d}{k_x}\right)\Sigma \tag{10}$$

From Eq. (10) , we find μ_d. The quantities mg and $k_z z_{off}$ are estimated from the experimental geometry. Also, the measured y-intercept of $\Delta x(t)$ versus F_C ($y - \text{int}_2$) gives

$$y - \text{int}_2 = \left(x_0 - \frac{(F_A + mg - k_z z_{off})\mu_d}{k_x}\right)\Sigma \tag{11}$$

In principle, either Eq. (9) or Eq. (11) can be used to obtain F_A. Hence, having values for m and γ, the experimentally determined parameters are ω, ω_o, k_x, μ_d and F_A. Examples will be given in the Dynamic Friction Data section below. In the data we report here, only Methodology B will be used.

IV.4 EXPERIMENT DESIGN

The tests described above were run on nanotractors from two different lots. The first was FP247, and the second was FP415. These are designations from the SUMMiT V^{TM} process [18]. Table I describes the experiment design:

Table I Friction Experiment Design

Split	Lot	Coating	Spring	rms (nm)			
1	247	FOTAS	A	7*			
2	247	Oct	A	7			
3	247	OTS	A	7			
4	247	CPD	A	7*			
5	247	Plasma	A	7*			
6	415	FOTAS	B	3			
7	415	Oct	B				
8	415	OTS	B				

* high particles, see Fig. 2(b)

As seen in Figs. 1(b) and 1(c), the nanotractor designs are slightly different on the two lots. Lot 247 was the first successful nanotractor design. Although the height of the friction feet above the substrate, z_{off}=0.5 μm is small, the friction feet were formed by a dimple layer, and were not nominally flat. The design in Lot 415 eliminated the dimple cut so that the friction foot would be perfectly flat, as can be seen in Fig. 1(c). This makes the analysis of real contact area more practical. However, this nanotractor would not be as useful as an actuator because it first has to descend z_{off}=2 μm (the sacOx 1 thickness) to make contact with the substrate.

It should also be noted that the spring designs are different in the two lots. In particular, load spring A on Lot 247 is a non-linear strain stiffening spring that allows a wide tangential force range (0-500 μN) to be explored. This was used to explore the applicability of Amontons'

First Law over a wide normal force range (0 to ~500/μ_s μN, where μ_s depends on the coating). (Explanation of these limits: The maximum force the actuator can deliver is 500 μN, and is limited by plate stretching. To ensure that the clamping force does not limit the actuator force, the normal load on the clamps must be ~500/μ_s μN). These nanotractors were also attached to a weak linear load spring that serves to keep its motion linear. Its small tangential force is included to obtain the total load spring force. The linear load spring also exerts a small out-of-plane force. For lot 247, this force is $k_z \bullet z_{off}$=0.64 N/m•0.85 μm =0.54 μN [6]. The differences between these load springs have been detailed [24]. Lot 415 used a medium stiffness (~3.5 N/m) linear load spring, spring B in Table I. The linear nature of the load spring allows us to implement the dynamic friction testing as described above. Given that the safe walking distance of these nanotractors was ~30 μm (walking past this point results in shorting of the actuation plate), the normal force range that could be explored with these nanotractors was narrower (0 to ~100/μ μN, where μ depends on the coating). (The safe walking distance was limited by a layout error that was later corrected so that the full ±100 μm could be realized). This linear load spring exerts a somewhat larger out-of-plane force of $k_z \bullet z_{off}$=3.5 N/m•2 μm =7 μN.

The rms roughness of the splits on both lots was also checked using tapping mode atomic force microscopy (AFM). A representative image of the lower counterface from Lot 415, with 2.8 nm rms surface roughness, is shown in Fig. 2(a). The appearance of the other splits was the same on Lot 415. On Lot 247, the rms roughness was somewhat larger at 7 nm rms. Splits 1, 4 and 5 all went through the release process together (common steps were HF release and CPD), and were all showered with particles, as is shown in Fig. 2(b). We realized this only after testing had been completed. Split 6 was also initially covered with particles. Four attempts over the year were made to obtain particle-free chips on this split. The first three failed, either due to release processing problems in the fab (mishandling), or because again there were very large particle counts. Finally, the fourth succeeded, and these parts were tested in the last week of September, 2005. Hence, Split 6 is clean, similar to Fig. 2(a).

V. RESULTS AND DISCUSSION

We now present results and discussion of the static and dynamic friction test data. We then demonstrate that the data correlates with AFM friction measurements. Finally we measure PSTD on two of the coatings, and further find creep-like behavior for OTS.

V.1 STATIC FRICTION TESTS ON LOT 247

Representative static friction data from Splits 1-5 are shown in Figs. 6-10. For each case, the raw data is shown from which the other plots are made. The raw data is taken by walking the nanotractor out to some distance x_0. It is then clamped with a voltage sufficiently large to hold it in place. The clamping force F_C is then gradually reduced (at 2 volts/sec, typically) while the nanotractor in-plane displacement, x, is monitored. As F_C is reduced, x exhibits slip events, Δx. When slips are very small, it is not clear whether the transition from static to dynamic friction has occurred or if the events are representative of PSTD, as discussed above. A slip event was defined as Δx>200 nm. This is well beyond the resolution of the metrology, which for these tests was ~ ±10 nm, to ensure that only static friction jumps (and not pre-sliding tangential deflections) are recorded in the friction data. Once the nanotractor returned near to the zero position, it was walked out to monotonically increasing x_0 values. This procedure ensured that the F_C space was filled out evenly. Furthermore, it ensured that the first tests were performed at the lightest normal loads in order to minimize any effect of wear. Wear can easily be inferred if the raw data in later tests does not overlap the earlier tests. With exceptions that will be noted, very good overlap of the raw data was seen.

As is seen in Fig. 6(a) for FOTAS, as x_0 increases, Δx tends to increase. This is because the inertia of the nanotractor increases as x_0 grows. The largest value is x_o ~23 μm, as limited by the load spring A. Otherwise, the raw data in Fig. 6(a) is typical. An x-offset is introduced between each x_0 run so that the data can be clearly distinguished. If the x-offset between the different traces is set to be zero, no overlap is observed.

The resulting static friction data for Split 1 is seen in Fig. 6(b). It is apparent that there is a slope change in the data for F_C>200 μN. Here, μ_s=0.236 ± 0.003 and μ_s=0.327 ± 0.010 for the lower (0-200 μN, r^2=0.961) and higher (200-2500 μN, r^2=0.990) F_c ranges, respectively. The uncertainties in the slope represent one sigma. Hence, the slopes clearly are statistically different from each other. The slope change could also be due to an artifact, because the calibration of the load spring, especially at low loads, is not known perfectly. However, while the form of the calibration curve makes it susceptible to absolute errors, its sensitivity to relative errors is small.

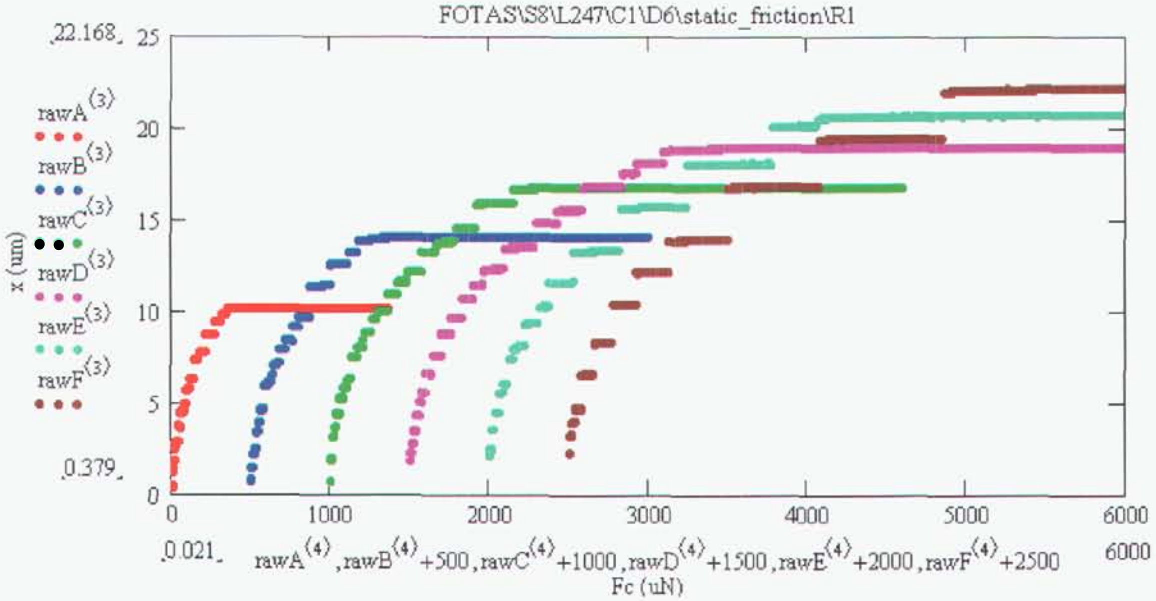

Figure 6(a) FOTAS static friction test raw data (Device 6). Different colors represent different x_0 values, and are offset by F_c=500 μN so that the curves can be distinguished.

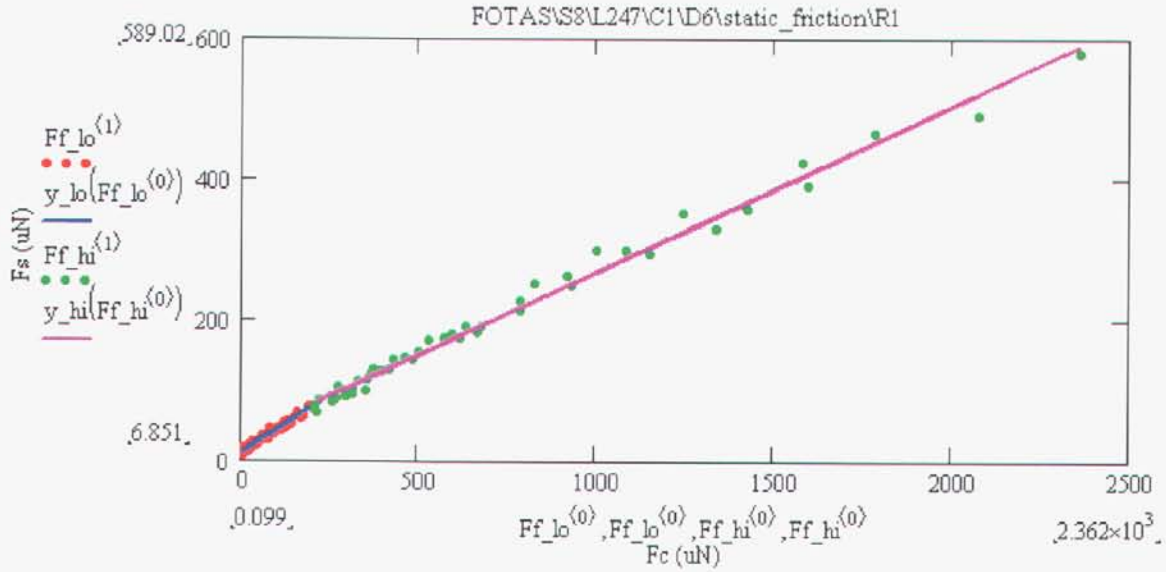

Fig. 6(b) FOTAS static friction results (Device 6). Here, μ_s =0.236 ± 0.003 and μ_s =0.327 ± 0.01 for the lower (0-200 μN, r^2 =0.961) and higher (200-2500 μN, r^2 =0.990) F_c ranges, respectively. Dots – data as extracted from static friction limits in Fig. 6(a), and Lines – linear fits to the data.

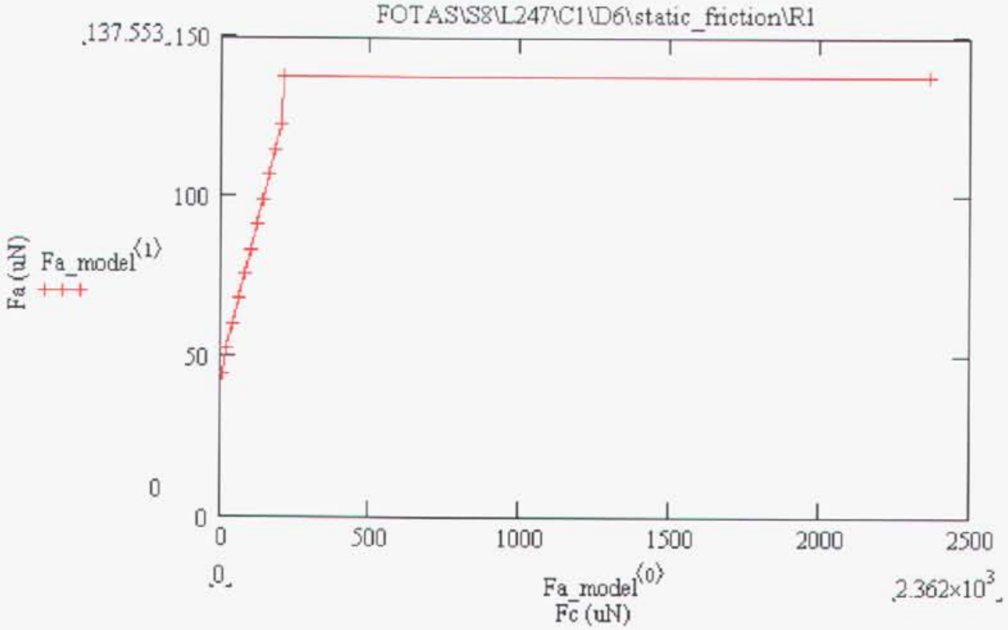

Fig. 6(c) FOTAS static friction test adhesion force (Device 6) versus normal load. To fit the static friction data over the entire load range, we take μ_s from the higher load range and allow F_A to vary with F_c in the low load range. At F_C=0 μN, F_A=40 0 μN.

Conceptually, there are two ways to consider the slope change. It could be that μ_s is decreasing as F_C decreases or that the adhesion force F_A increases as F_C increases. If contact between the surfaces occurs at only one point, then we would expect the former case. That is, if we assume shear strength is independent of load, single asperity contacts would show this trend [38]. However the surface most likely consists of multiple contacts, which are at different heights. Well-known models such as the Greenwood-Williamson (GW) model then show that the area is proportional to the number of contacts [43,44]. In fact, extensions of this model show that adhesion should increase with normal load because the real contact area increases [45]. We take the latter view here, and in Fig. 6(c), we show a fit of F_A versus F_C. With a single value of μ_s=0.236 from the high load range, all the data is well described. Hence, we have modified Eq. (2) to take the form

$$F_s = \mu_s(F_c + mg - k_z z) + \mu_s F_A(F_c), \tag{12}$$

From the fit, F_A is approximately linear with F_C until it reaches a saturation value. Its *y*-intercept is clearly different from zero, indicating that friction exists as zero applied load, as previously reported [6,46]. Note that just before F_A reaches saturation at F_C=200 μN, it experiences a somewhat abrupt change. This is merely because the fit over the wide range of higher normal loads is assumed to be perfectly linear down to F_C=200 μN, whereas the data is slightly below this. A more thorough analysis would take into account the small downwards curvature of the data in the high load range.

Static friction results from Lot 247 for an octadecene coating are shown in Fig. 7. The raw data in Fig. 7(a) is qualitatively similar to Fig. 6(a) for FOTAS, except that the static to dynamic friction jumps as the test progresses to higher x_o values is not as large as in Fig. 6(a). Again in the static friction results in Fig. 7(b), we see a slope change from μ_s=0.253 to μ_s=0.168 at F_C=500 μN, which is statistically significant. Here, the surface particles are very much reduced, so the slope change now cannot be due to a processing artifact. Fig. 7(c) shows the fit for $F_A(F_C)$. It is also worthwhile to note that the normal load range in Fig. 7(b) is larger than Fig. 6(b) because the μ_s is now smaller, as explained in the EXPERIMENTAL section.

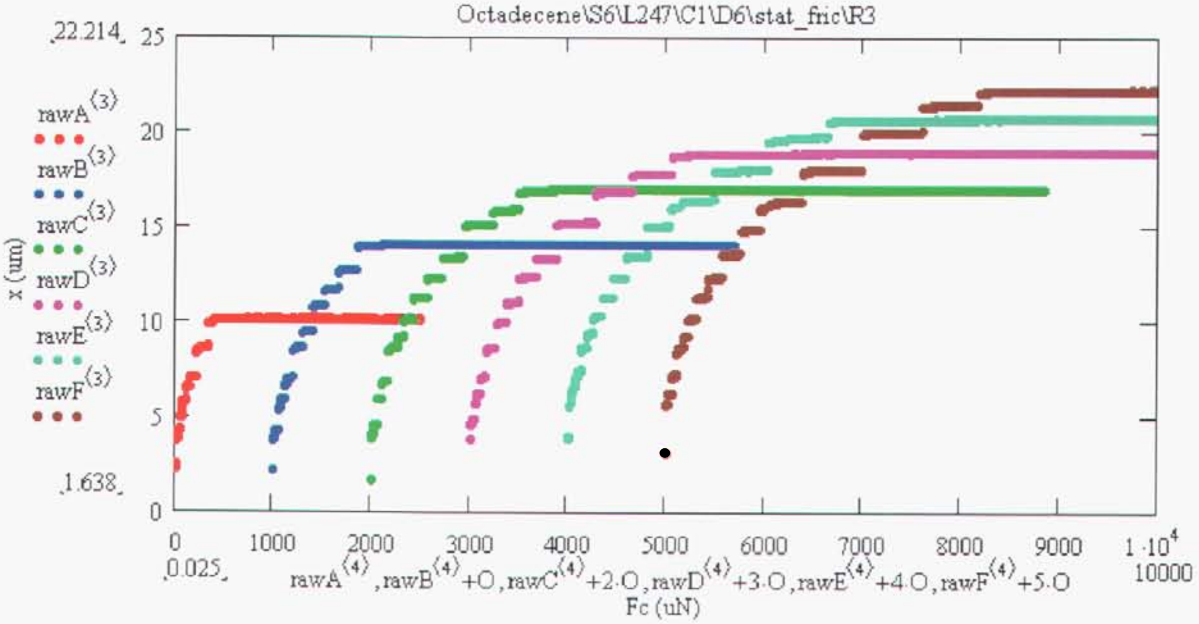

Figure 7(a) Octadecene static friction test raw data (Device 6). Different colors represent different x_0 values, and are offset by F_c=1000 μN so that the curves can be distinguished.

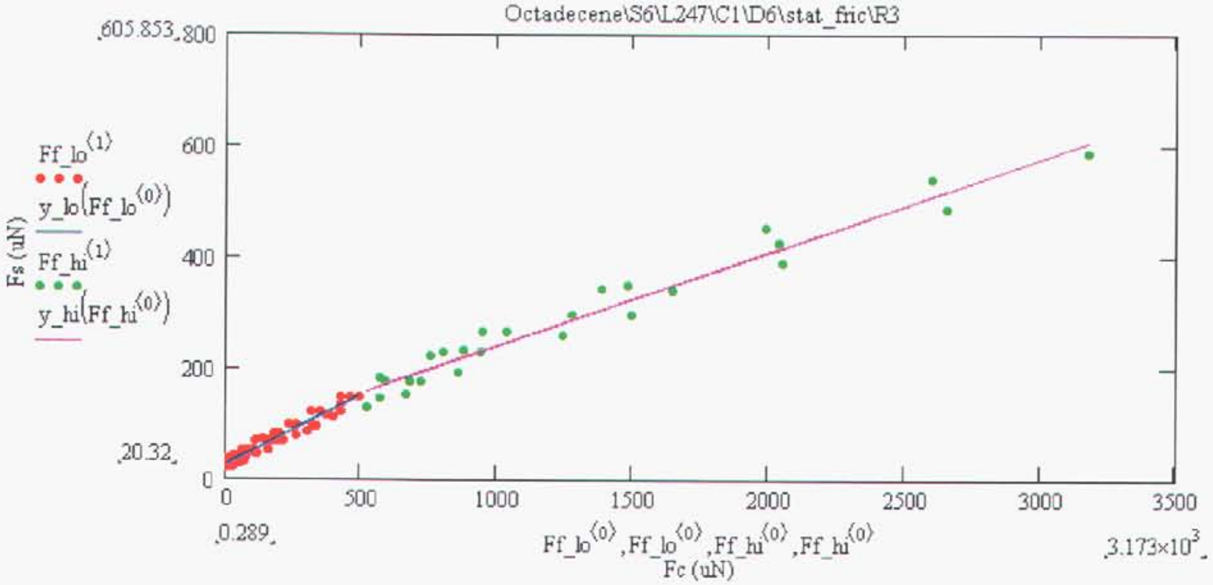

Figure 7(b) Octadecene static friction results (Device 6). Here, μ_s =0.253 ± 0.009 and μ_s =0.168 ± 0.007 for the lower (0-500 μN, r^2 =0.940) and higher (500-2500 μN, r^2 =0.961) F_c ranges, respectively. Dots – data as extracted from static friction limits in Fig. 7(a), and Lines – linear fits to the data.

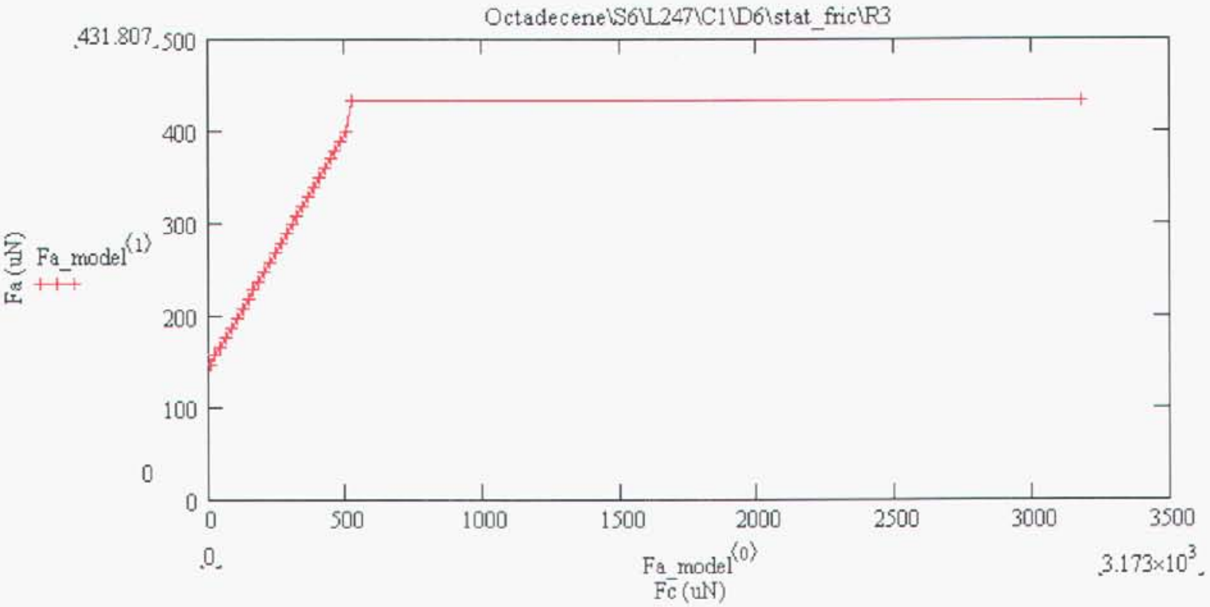

Figure 7(c) Octadecene static friction test adhesion force (Device 6) versus clamping load. To fit the static friction data over the entire load range, we take μ_s from the higher load range and allow F_a to vary with F_c in the low load range. At F_C=0 μN F_A=150 μN.

In Fig. 8 we see static friction results from Lot 247 for an OTS coating. The raw data in Fig. 8(a) is qualitatively similar to Fig. 7(a) for octadecene. The friction data in Fig. 8(b) again shows two different slopes. Although the slope differences are again statistically significant, there appears to be more downwards curvature in the higher load range (F_C>200 μN). Fig. 8(c) shows the $F_A(F_C)$ trend. Fig 8(d) shows that the OTS raw data does not have a memory effect for lot 247 as all measurements appear to line up. This will be seen to in sharp contrast with Lot 415.

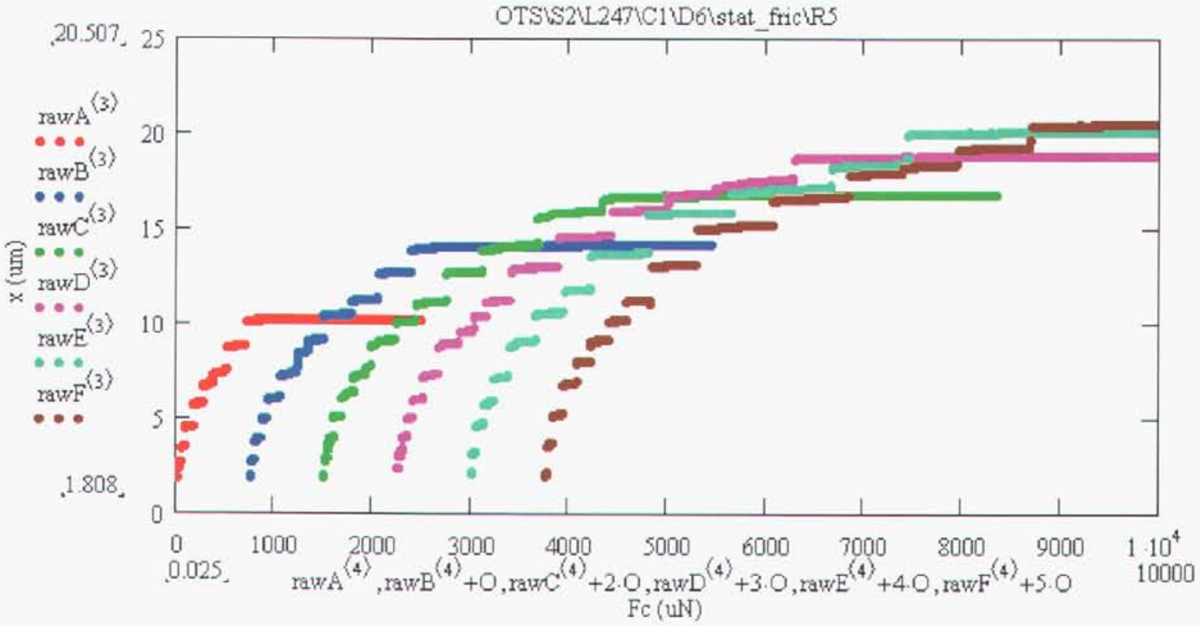

Figure 8(a) OTS static friction test raw data on lot 247. Different colors represent different x_o values, and are offset by F_c=750 μN so that the curves can be distinguished.

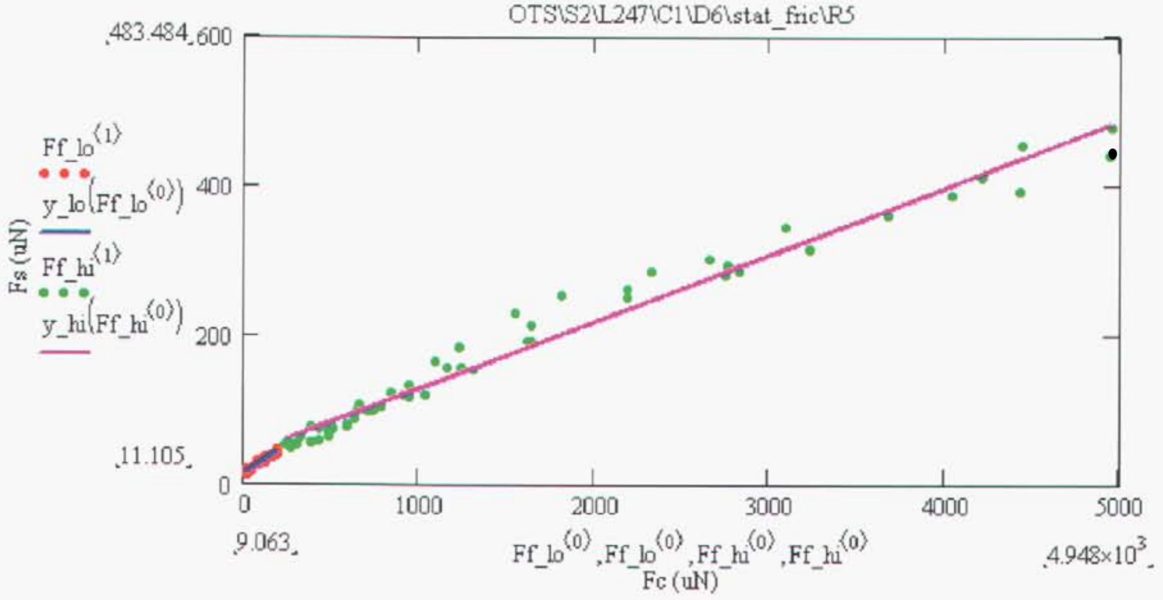

Figure 8(b) OTS static friction results (Device 6). Here, μ_s =0.090 ± 0.002 and μ_s =0.164 ± 0.009 for the lower (0-200 μN, r^2 =0.935) and higher (200-5000 μN, r^2 =0.976) F_c ranges, respectively. For the overall fit, μ_s =0.090 and F_a varies with F_c per the following figure. Dots – data as extracted from static friction limits in Fig. 8(a), and Lines – linear fits to the data.

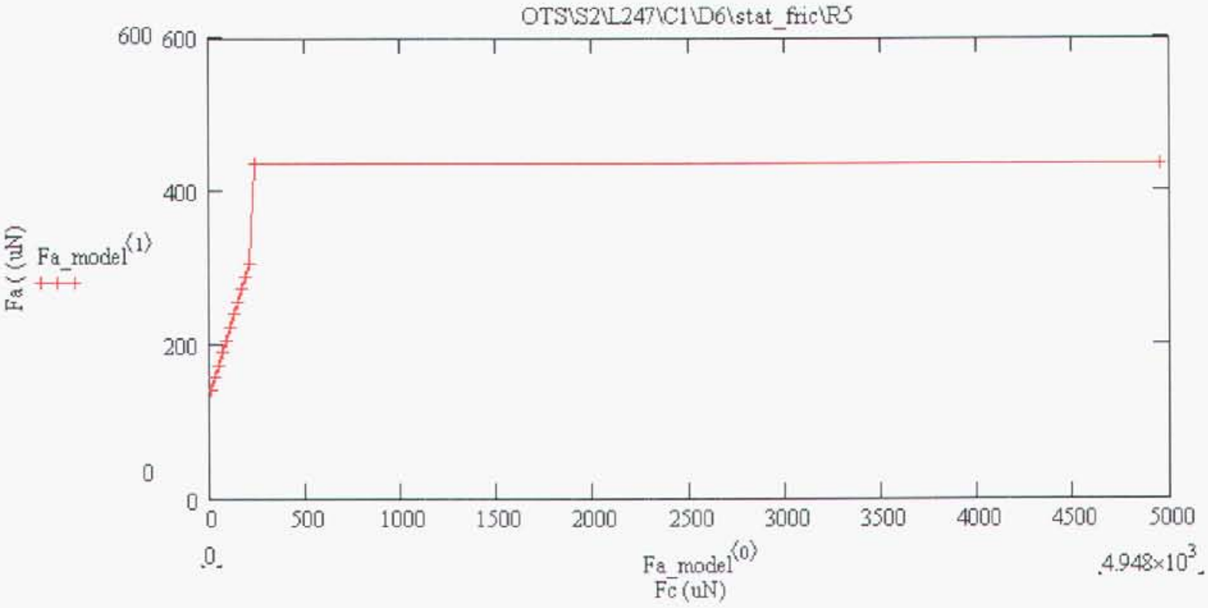

Figure 8(c) To fit the static friction data over the entire load range, we take μ_s from the higher load range and allow F_A to vary with F_c in the low load range. At F_C=0 μN, F_A=150 μN.

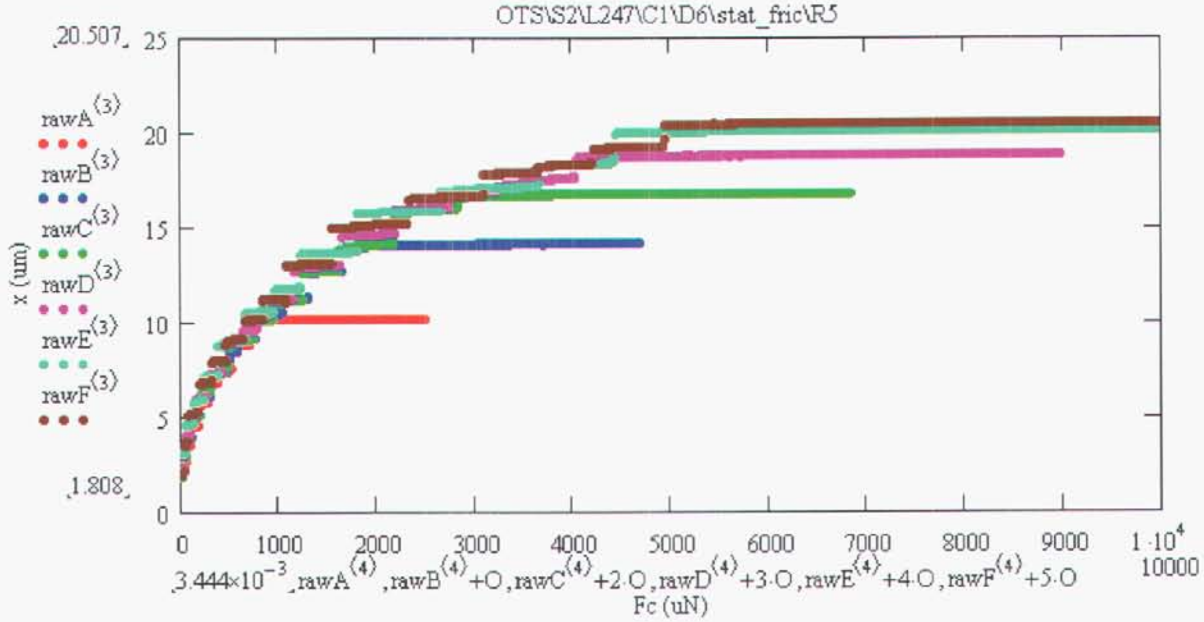

Figure 8(d) Same data as Fig. 7(b), but color coded by x_o values. This is to show that the friction data are only dependent on x_o.

The results for the CPD in Fig. 9 show some differences from the FOTAS data in Fig. 6. The raw data in Fig. 9(a) shows static large jumps, indicating that the dynamic friction is substantially less than the static friction. It also shows some tendency to jump to a previous position as x_o increases. This is indicative possibly of a history effect, or of local differences in adhesion. The friction data in Fig. 9(b) does not indicate any difference in slope, nor was any such difference statistically valid. Here, μ_s=0.236 ± 0.002 (r^2=0.996), and F_a=39.3 ± 1.6 μN for all the data. These values are quite similar to those of FOTAS.

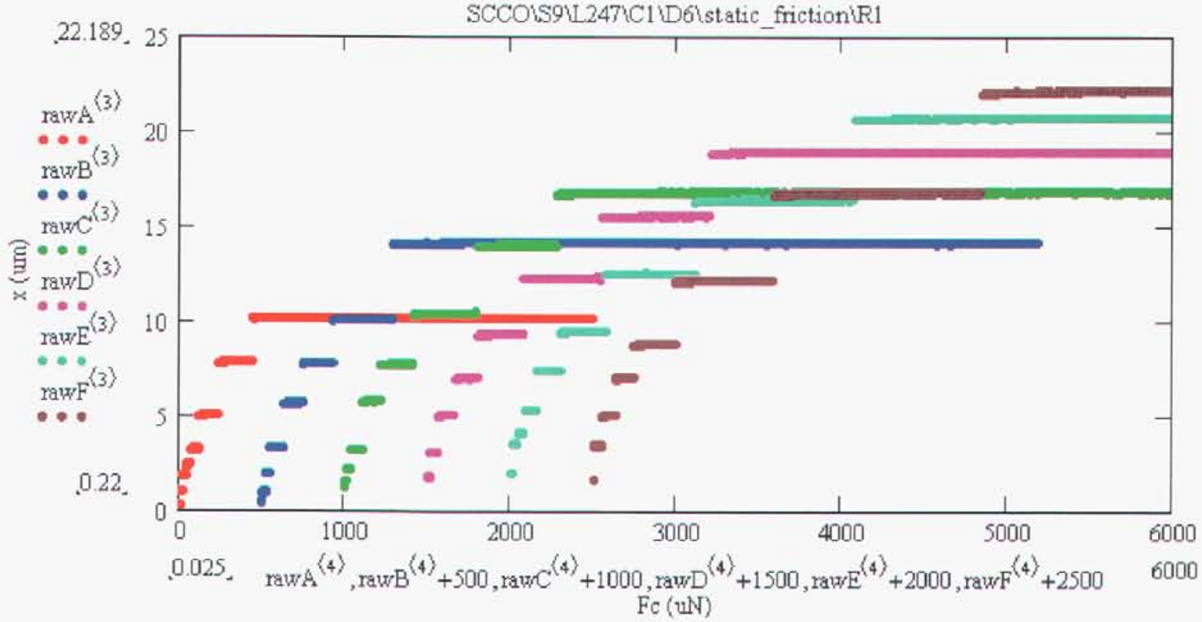

Figure 9(a) CPD static friction test raw data (Device 6). Different colors represent different x_0 values, and are offset by F_c=500 μN so that the curves can be distinguished.

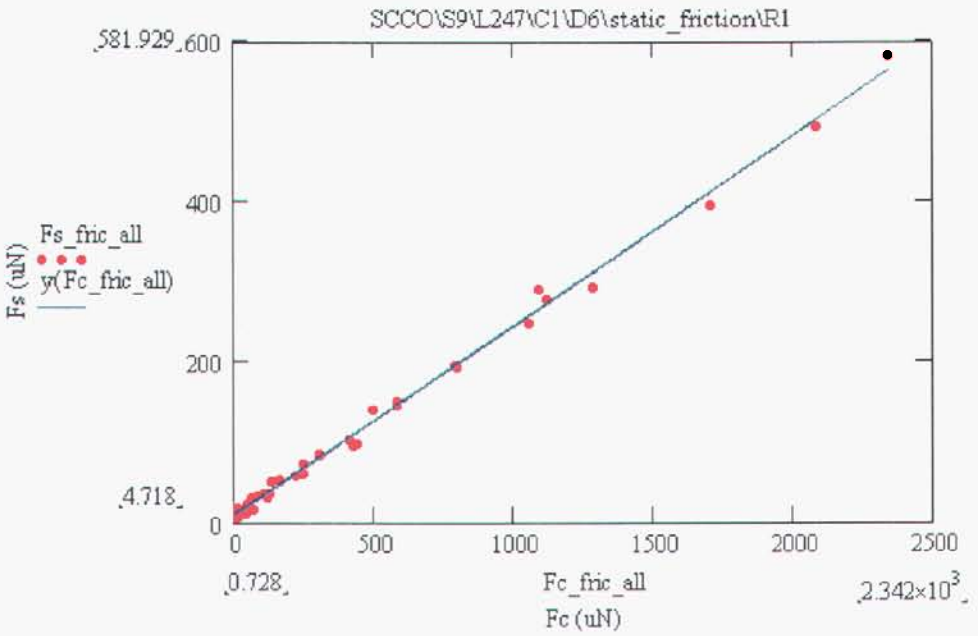

Figure 9(b) CPD static friction results (Device 6). Here, μ_s=0.236 ± 0.002 (r^2=0.996), and F_a=39.3 ± 1.6 μN for all the data (there is no distinction between the lower and upper load ranges). Dots – data as extracted from static friction limits in Fig. 9(a), and Line – linear fit to the data.

The final graph for static friction results from Lot 247 are shown in Fig. 10 for a plasma-cleaned surface. Initially the friction is already higher with μ_s=0.524 ± 0.012 as seen in Fig 10(a). After the plasma clean, the sample remained in vacuum for a few hours, but was tested within 10 minutes after removal from the chamber. This sample showed a strong time-dependent effect. After only 30 more minutes in air, adhesion was very high and only friction jumps occurred only for a few points, as seen in Fig. 10(b). An image of an adhered nanotractor holding off a tangential load of ~500 μN with zero clamping voltage is seen in Fig. 10(c).

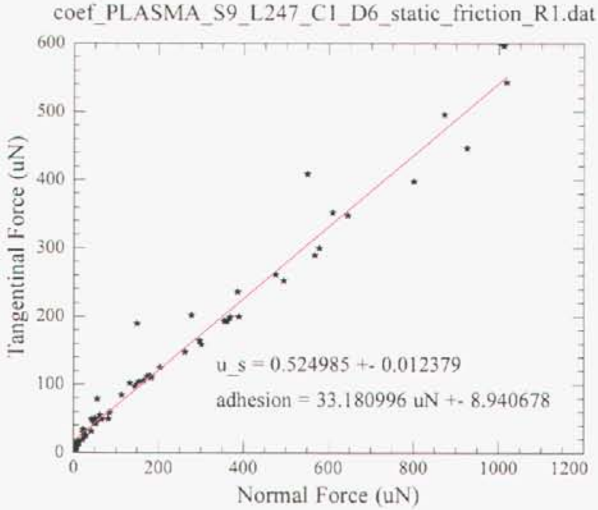

Figure 10(a) SCCO static friction results (Device 6). Here F_a =33.3 ± 8.9 μN for all the data (there is no distinction between the lower and upper load ranges). Dots – data as extracted from static friction limits in Fig. 9(a), and Line – linear fits to the data.

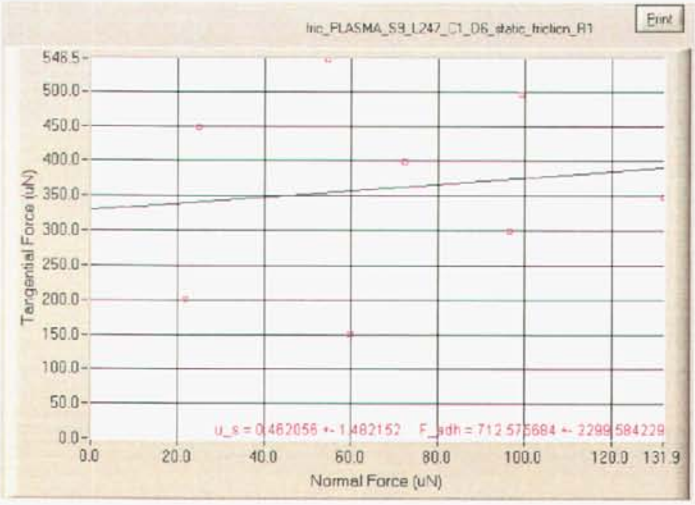

Figure 10(b) SCCO static friction results 30 minutes later. The device is sticking due to adhesion.

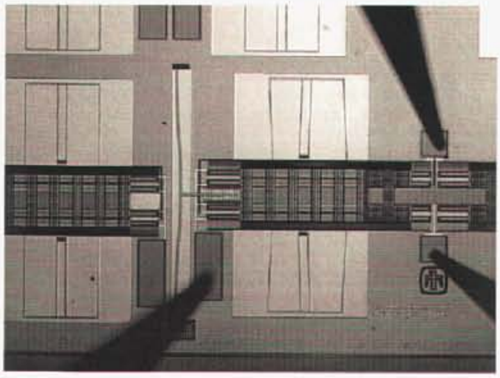

Figure 10(c) The nanotractor remains in place due to adhesion only.

In summary for this section, we show in Fig. 11 and in Table II averaged results for multiple tests. These results are for 2 different devices with ~ 6 – 10 measurements from each coating. The μ_s data in Fig. 11(a) are taken as the average over the full range, and the F_A data in Fig. 11 (b) are the saturation values also from the full load range. Overall, $\mu_{s,OTS} < \mu_{s,Octadecene} < \mu_{s,CPD} < \mu_{s,FOTAS} < \mu_{s,Plasma}$. This is in accord with expectations from our earlier discussion on the friction of monolayers. Evidently, the CPD contamination layer is roughly as lubricious as the FOTAS coating when averaged over all the data. Although μ_s is the lowest for OTS, F_A is the highest for this coating. Conversely, for FOTAS, while μ_s is high, F_A is low. This suggests that although the surface energy for FOTAS is low because it consists of low-surface energy fluorocarbons, the disorder in the chains leads to a high μ_s. Clearly, it is important to apply Eq. (2), which takes into account both F_A and μ_s, to best estimate the friction. Although not included in Fig. 11 or Table II, it also appears that F_A depends on F_C for the coated nanotractors per Eq. (12), but not for the uncoated nanotractors.

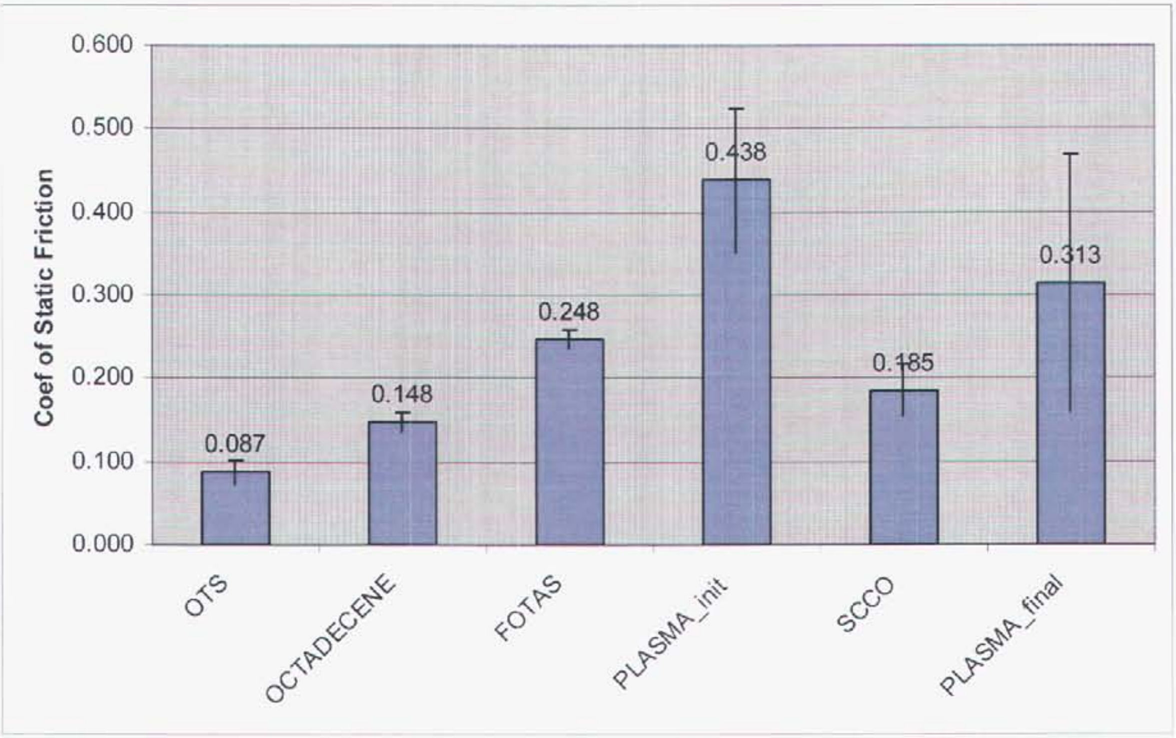

Figure 11(a) Summary of friction data (see table 2 for details)

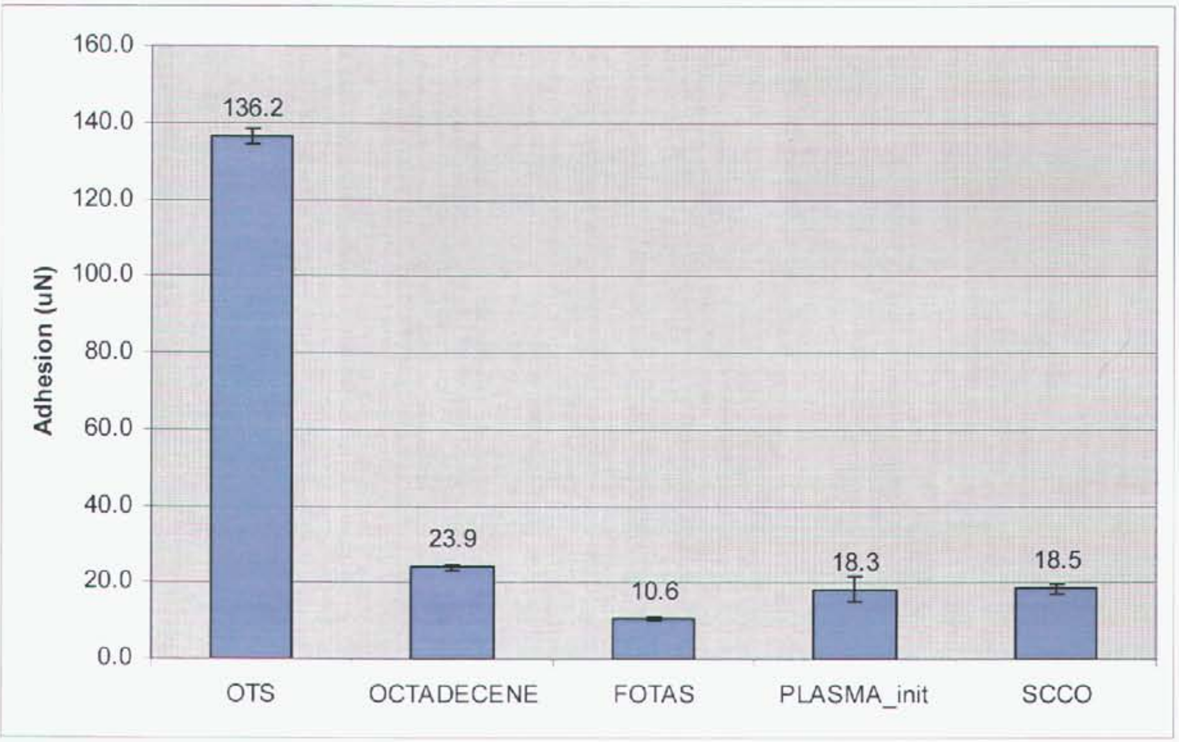

Figure **11(b) Summary of adhesion data. PLASMA_FINAL not plotted as it is off chart (see table 2 for details)**

At present, these numbers and conclusions must stated tentatively because the FOTAS, CPD and Plasma-treated nanotractors all had very high particle counts as seen in Fig. 2(b). We will be repeating this experiment for the data in question so that our confidence will be improved.

Table II Lot 247: μ_s and F_A statistics

Coating	μ_s	μ_s st. dev.	μ_s % error	F_A (μN)	# meas.
FOTAS	0.248	0.024	9.6	10.6	6
OCTADECENE	0.148	0.023	15.4	23.9	7
OTS	0.087	0.031	35.3	136.2	10
PLASMA_INIT	0.438	0.08	16.9	18.3	2
PLASMA_FINAL	0.312	0.154	49.4	1582	2
CPD	0.185	0.063	33.9	165.9	8

V.2 DYNAMIC FRICTION DATA

We present the dynamic friction data in this section for Splits 6 and 8 from Table I (insufficient devices were available to take data on octadecene). According to Eq. (7c), $\Delta x(\Delta t)$ vs x_o should be linear if Eq. (5) accurately describes the dynamic response of the nanotractor. Data for FOTAS (with F_c=0 μN and Δt=42 μsec) shown in Fig. 12(a) with r^2=1.000 indicate that this is so. The slope of $\Delta x(\Delta t)$ vs x_o can be used to determined ω. In practice, Eq. (8b) is used to estimate ω by assuming γ=0 and α=0. Then ω is solved exactly by iteration assuming γ=3.61•10^3/sec [6], and with the known dependence $\alpha(\omega)$. The results are ω=4.300•10^4/sec, which in turn gives ω_o=4.304•10^4/sec and k_x=4.168 N/m using mg=0.022 μN [6]. Then we find Σ=1.138.

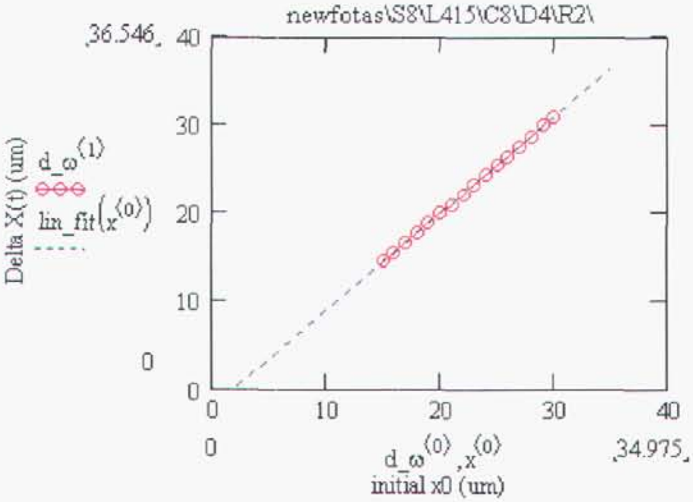

Figure 12(a) Dynamic frequency data ($\Delta x(\Delta t)$ vs x_o with F_c=0 μN and Δt=42 μsec) for FOTAS coating on lot 415. For this data, r^2=1.000. The slope of this plot gives ω=4.300·10^4/sec, which in turn gives ω_o=4.304·10^4/sec. Then k_x=4.168 N/m.

Furthermore, $\Delta x(F_C)$ vs x_o is also linear in Fig. 12(b) with r^2=0.999. From Eq. (10), the slope of this line=-9.8•10^{-3} μN/μm can be used to find μ_d=0.135. Finally, the y-intercept of Fig. 12(b), $y-\text{int}_2$=31.5 μm, and Eq. (11) give F_A=78.5 μN, where we have estimated $k_z z_{off}$=6.5 μN. (It is also possible to use Eq. (9) and $x_o-\text{int}_1$ from Fig. 12(a), but it is not possible to take the data close to the intercept, so $y-\text{int}_2$ is preferred).

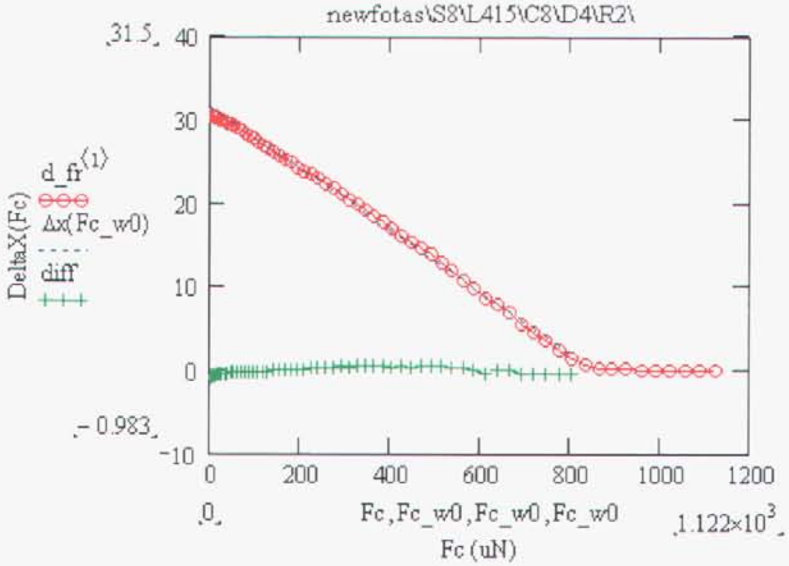

Figure 12(b) Dynamic friction data ($\Delta x(F_c)$ vs F_c with x_o =30 μm and Δt =42 μsec). The slope of this line gives μ_d. The green line is the difference between the linear regresion fit and the data. The y-intercept gives F_a.

With the constants known, we now plot Eq. (3) in Fig. 12(c). Static friction data was taken on the same device and is also shown. We note that in general $F_d < F_s$, in accordance with the third law of friction. For low F_c values, F_d appears to be larger than F_s, but due to noise in the static friction data, there is no effect statistically. It should also be noted that the particle-free data in Fig. 12(c) for FOTAS shows lower friction than the dirty surface in Fig. 6(b).

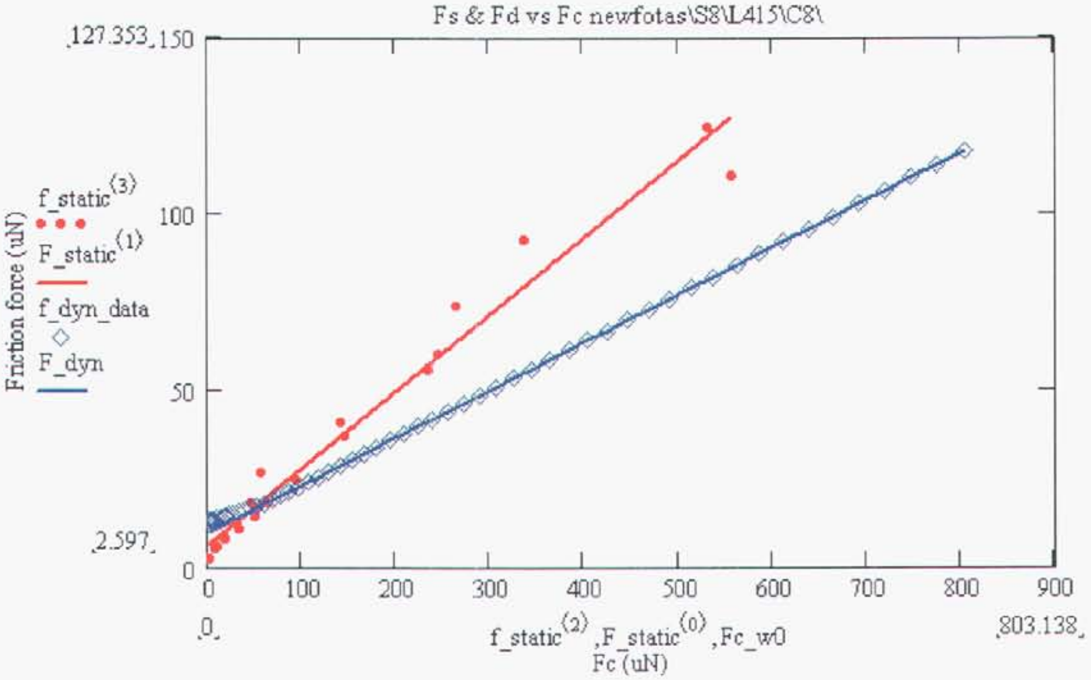

Fig. 12(c) Dynamic and static friction versus F_c for FOTAS from lot 415. The range of F_c values is not as large as the data from lot 247 because we are using a weaker load spring, and the range of the range of the device is only ± 40 μm. Perhaps because of this smaller range in F_c, there is no distinct slope change for the static friction data. For low F_c values, F_d appears to be larger than F_s, but due to noise in the static friction data, there is no effect statistically. Using a constant slope and adhesion, for dynamic friction μ_d =0.135 and F_a =78.5 μN, while for static friction μ_s =0.217 and F_a =35.9 μN.

The $\Delta x(\Delta t)$ vs x_o data for OTS in Fig. 13(a) also is linear with a high r^2 value. The values ω_o =4.285·10^4/sec and k_x =4.132 N/m are close to those for the FOTAS data in Fig. 12(a) as expected for mechanical parameters from chips on the same wafer. However, the $\Delta x\,(F_C)$ vs x_o data in Fig. 13(b) is decidedly non-linear. Similar to the static friction data for FOTAS, octadecene and OTS (Figs. 6-8), this data has been fit in Fig. 13(c) with a constant value of μ_d from the high load regime and by varying F_A in the low load regime.

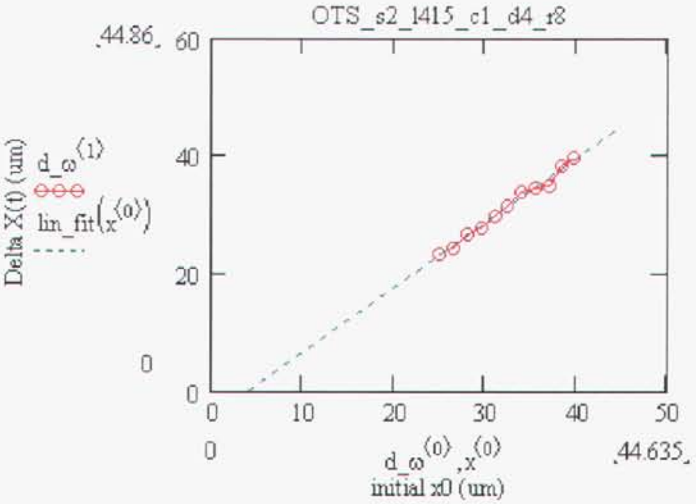

Figure 13(a) Dynamic frequency data ($\Delta x(\Delta t)$ vs x_o with F_c=0 μN and Δt=42 μsec) for FOTAS coating on lot 415. For this data, r^2=0.979. The slope of this plot gives ω=4.282·10^4/sec, which in turn gives ω_o=4.285·10^4/sec. Then k_x=4.132 N/m.

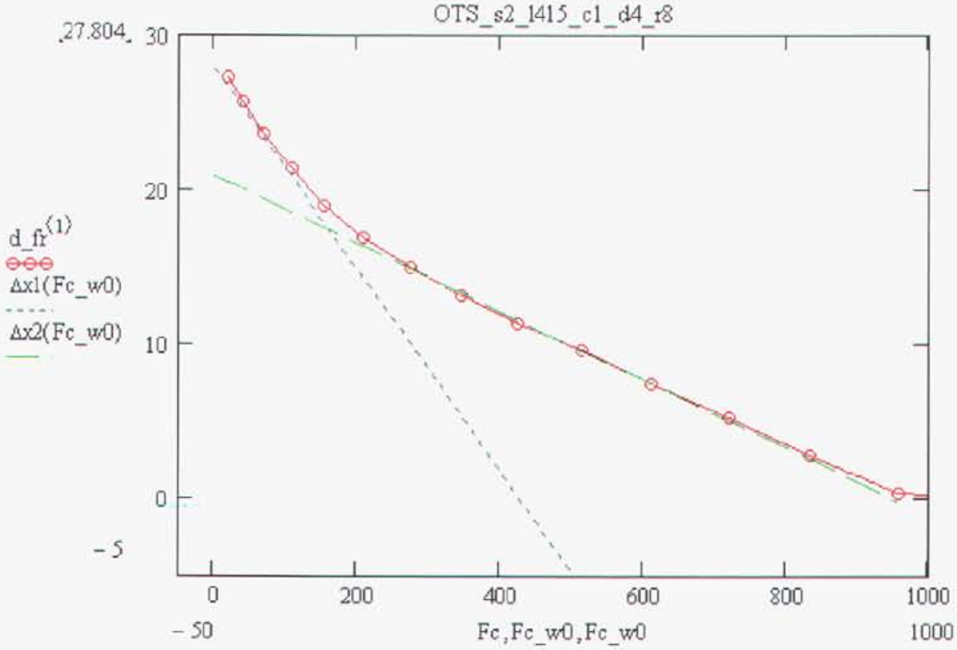

Figure 13(b) Typical OTS data for $\Delta x(\Delta t)$ versus F_c, from which μ_d is determined. The curve can be approximated by a linear fit in two regions.

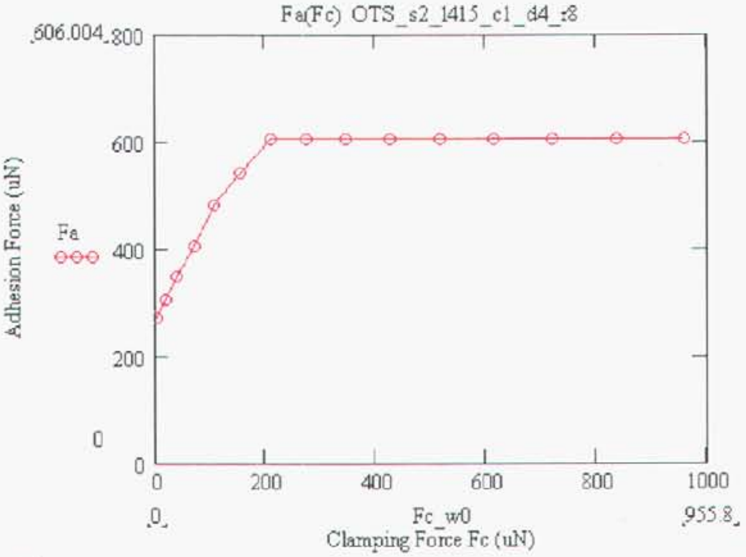

Figure 13(c) Values of F_a to match the friction data in Fig. 13(b) using μ_d =0.077 from the high load regime.

The F_d versus F_c trend is shown in Fig. 13(d), along with the F_s versus F_c trend. For both F_s and F_d, the data appears to depend on the initial position, x_o. Moreover, the value of x_o appears to control F_s and F_d to the same degree. That is, for the dynamic data, the x_o value lies between two x_o values for the static data, and the F_d values lie between the associated F_s values. Looking to Fig. 13(e), we see that the raw data also strongly depends on x_o. This is in contrast to the raw data for OTS on Lot 247, where the dependence in Fig. 8(d) is quite weak. The particle density for the OTS coating on both Lot 247 and Lot 415 is low. The reason for the apparent memory effect is unclear at this point. However, apparently F_s and F_d are very nearly equal for the same initial conditions.

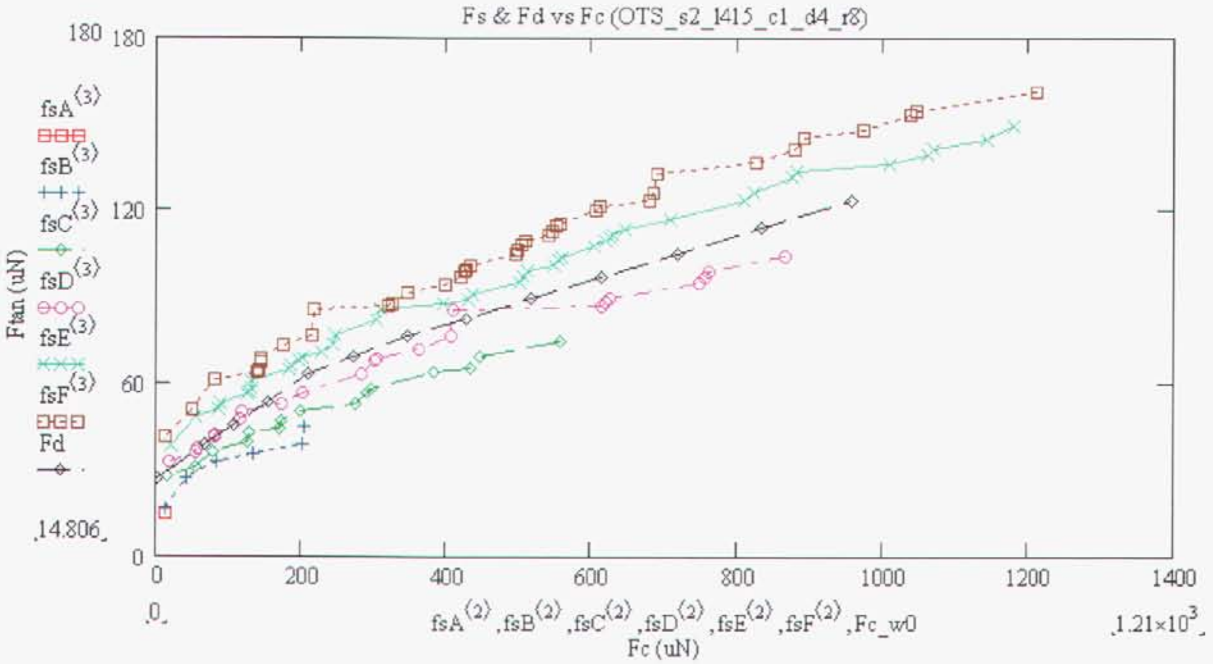

Figure 13(d) Dynamic (black) and static friction (other lines) versus F_c for OTS from lot 415. Here, both μ_s and μ_d clearly depend on F_c. Bizarrely, the static friction appears to depend on the x_o value. We have no explanation for this, but will look closely to see if this happens again. The x_o value for the dynamic data is between two x_o values from the static friction data, and all the dynamic friction data trends between these data.

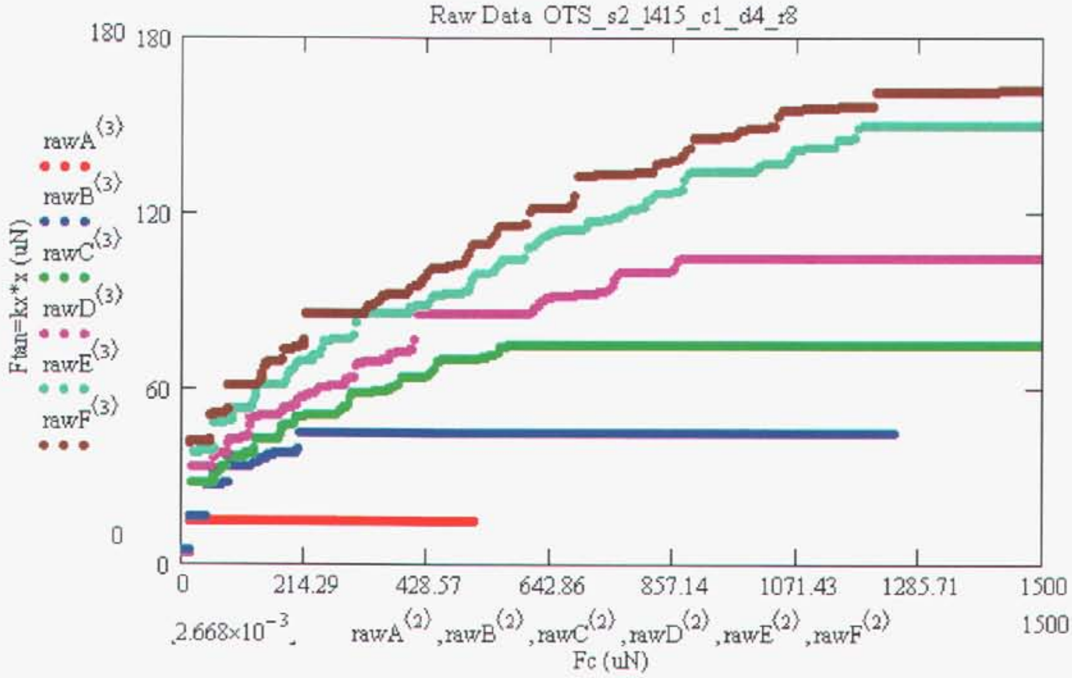

Figure 13(e) Typical raw data for OTS static friction plot. Note that the friction tends to increase as the nanotractor initially walks further out. This figure should be compared to Fig. 8(d).

The μ_d data are summarized and compared to the μ_s data in Fig. 14. The plotted data represents an average of measurements performed on two chips for each coating.

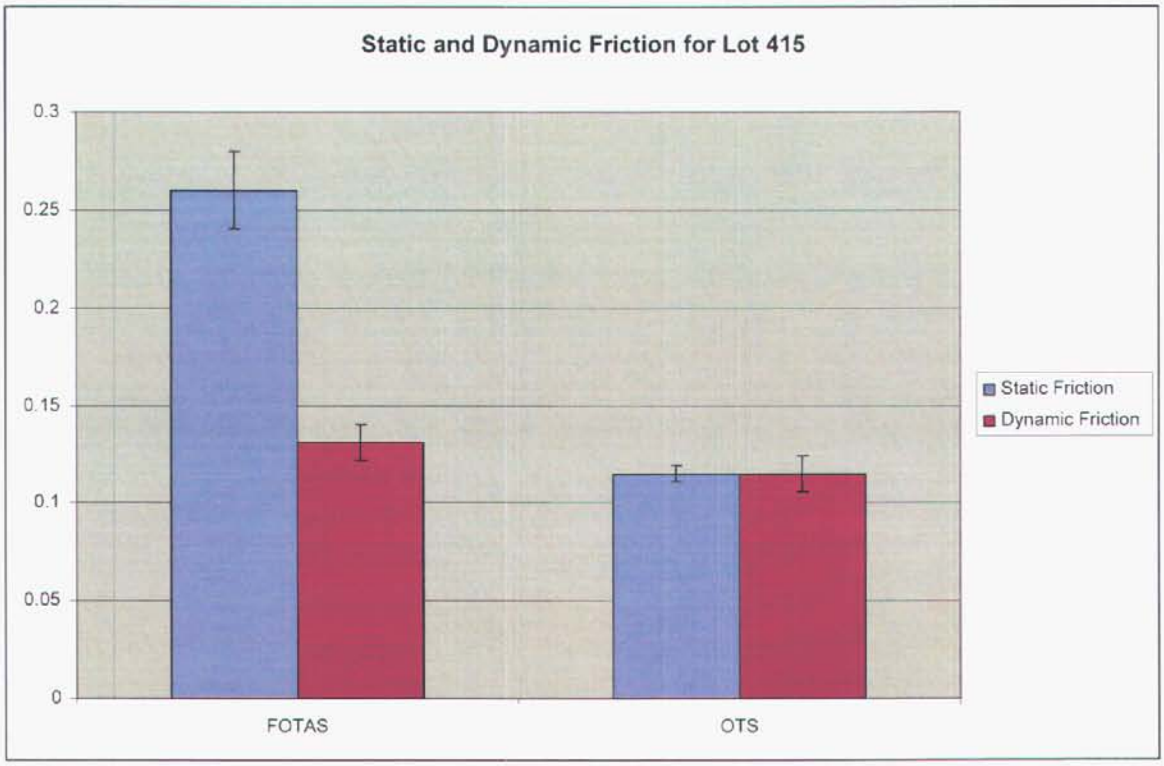

Figure 14 Static and dynamic friction coefficients for FOTAS and OTS from LOT 415. Data is taken from two chips for each coating.

V.3 AFM FRICTION FORCE MICROSCOPY

We conducted friction force microscopy of the interfaces using AFM tips on single crystal silicon substrates, both of which were co-deposited with the nanotractors. There are several reasons for performing these measurements. First, we would like to determine if the single asperity measurements explain the friction trends observed in the multi-asperity MEMS interfaces. Second, these measurements are required to validate model-based constitutive laws. Third, with the constitutive laws and a detailed knowledge of the interface, we would like to predict the friction of the MEMS interface and derive detailed information on local contact pressures and real contact areas. Fourth, we would like to see what behavior cannot be predicted from AFM measurements. In such cases, we expect that the multi-asperity nature of the interface must be taken into account.

Generally, the surfaces were featureless. However, because of the LC and LE phases in OTS, features in that monolayer were visible. The flower patterns in Fig. 15 are especially well seen in the friction force image on the right hand side, and indicate that a good monolayer was deposited. (There are a few particles on the surfaces, which could be due to a small-scale molecular agglomeration. The single asperity friction experiments are always performed well-away from theses particles.)

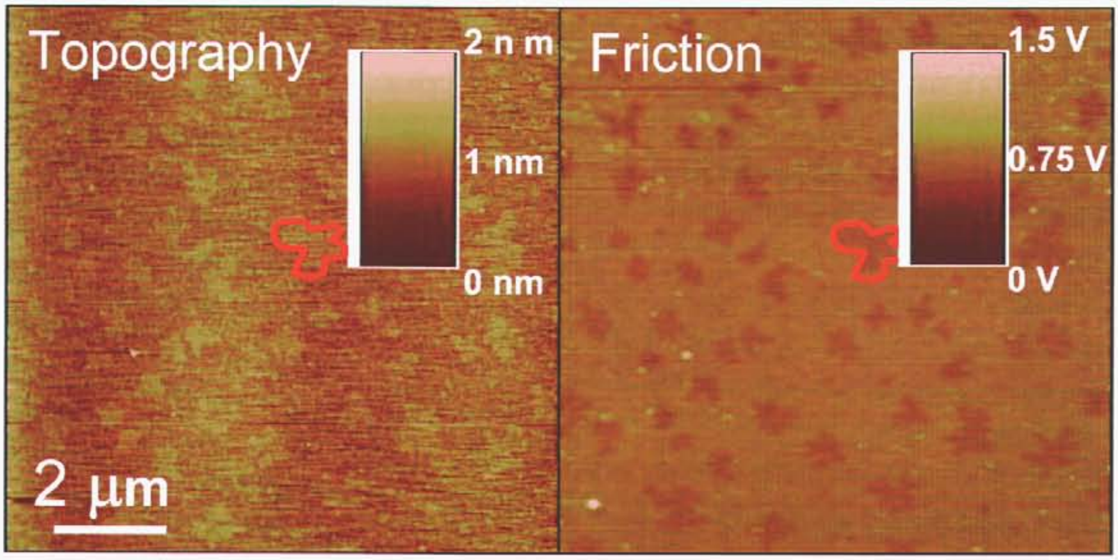

Figure 15 AFM topographic and friction force images of OTS on single crystal Si sample co-deposited with the nanotractors. The "flowers", which are better seen in the friction force image, are LC areas that are surrounded by LE areas. From the topographic image, it is apparent that the LE areas are slightly lower than the LC areas, indicating that LE areas are not fully dense.

Single asperity friction forces curves for OTS/OTS and FOTAS/FOTAS, as seen in Fig. 16, indicate that the friction in the former interface is lower than that of the latter. The AFM tip sizes for these data were R~40nm for FOTAS data R~36nm for OTS, as measured using TEM shadow profiles of the tips. The AFM trend correlates well with the multi-asperity data from the MEMS interface. Fig. 16 also shows that the friction is approximately the same on the LC and LE areas.

OTS/OTS vs FOTAS/FOTAS

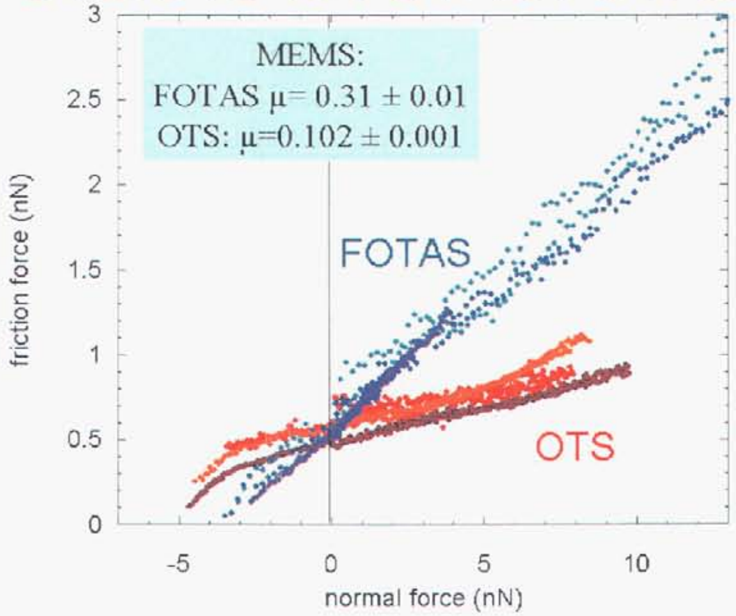

(a)

see also: S. Perry & co-workers

Differences in friction between the OTS phases also occur using an OTS-coated tip

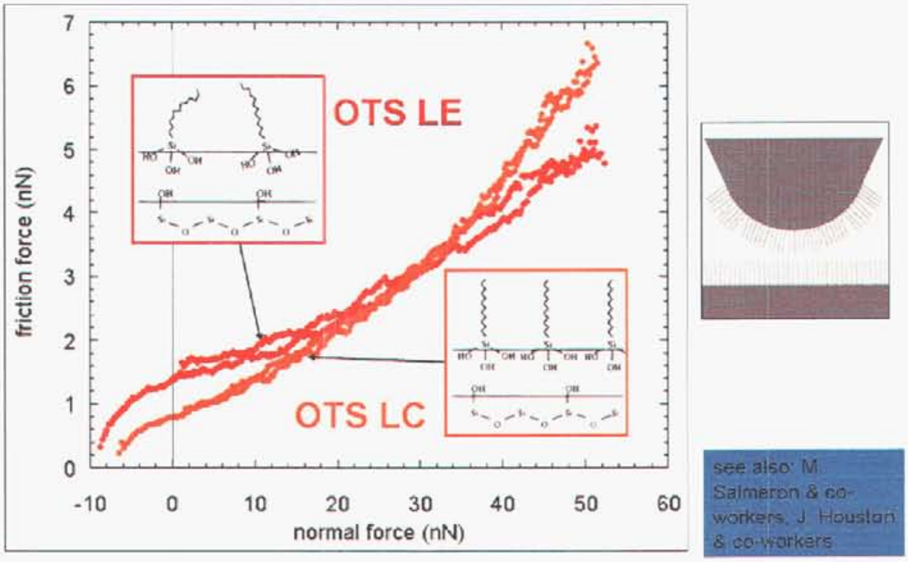

see also: M Salmeron & co-workers, J. Houston & co-workers

(b)

Figure 16 Single asperity data comparing OTS and FOTAS. (a) The friction is much lower for OTS than FOTAS. (b) the OTS data tends to curve up with normal force. This perhaps can be correlated to the increases in F_a with F_c as in Fig. 13(c).

V.4 SLIP BEFORE TRANSITION FROM STATIC TO DYNAMIC FRICTION

The inset of Fig. 17 shows friction data from an FOTAS-coated nanotractor from lot 247. Recall that the data begins in the upper right hand corner. The voltage is ramped down at a rate of 2 V/sec in this plot. As the normal force is lowered, there are well defined critical points at which the nanotractor jumps forwards by several microns or more. For this coating we find μ_s=0.31 ± 0.01 and μ_d=0.265 ± 0.005. The significant difference between static and dynamic friction leads to the well defined jumps.

If we examine the data in the main part of Fig. 17, we see that prior to the jump, slip events totaling 100 nm occur. This slip has been called "pre-sliding tangential deflections" (PSTD) in the tribology literature and is typically on the order of 100 nm. The data shows that we can resolve the fine structure of the pre-sliding events. The slip depends on the normal load, and the data suggests that local asperity interactions govern its behavior. The slip motion for the FOTAS coating is observed within one video frame (1/15th second) after the voltage is lowered and remains stable for 10 minutes. (At longer times we are sensitive to drift due to thermal instability of the test apparatus). We shall analyze this structure in the Mechanics Model section below.

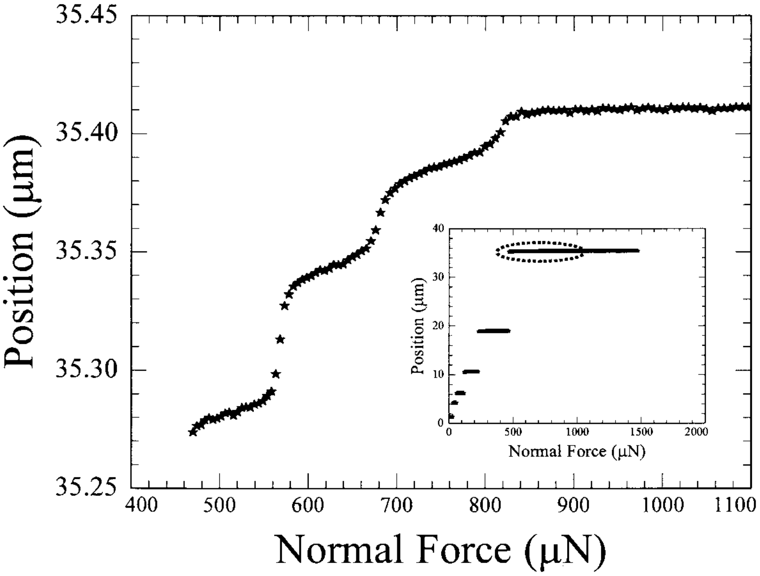

Figure 17 PSTD in an FOTAS treated nanotractor (Split 1). Data is from dotted region in the inset, which shows the large scale behavior.

Figure 17 shows a magnified portion of the position versus voltage curve of a lot 247 CPD-dried nanotractor (the data in the dotted circle of Fig. 18). We again observe that substantial slipping (80 nm) occurs before the gross sliding event and also the fine structure in the PSTD behavior. For this coating we find μ_s=0.27 ± 0.01 and μ_d=0.185 ± 0.01. The larger difference between static and dynamic friction leads to the emergence of only one jump (of many μm) as seen in the Fig. 18 inset, and again allows a clear separation of the gross slip and the much smaller PSTD events. We can thus again unambiguously attribute the fine structure to PSTD.

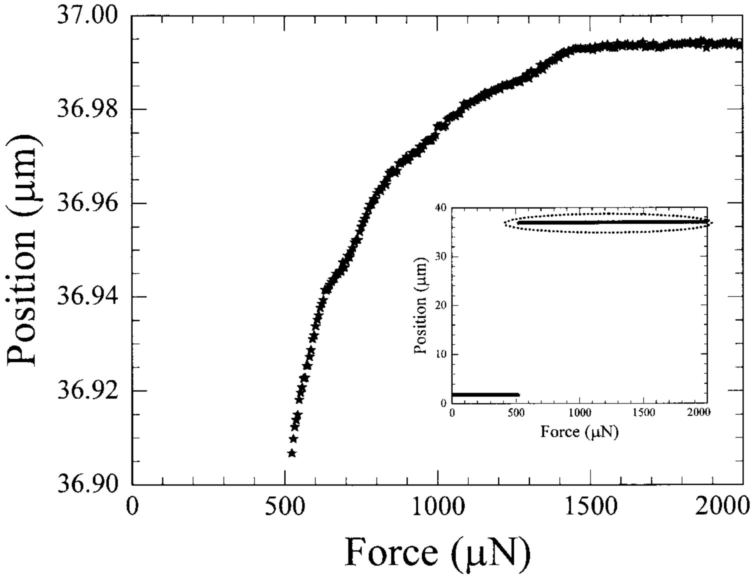

Figure 18 STD in a CPD-treated nanotractor. Data is from dotted region in the inset, which shows the large scale behavior.

The PSTD is important in applications where we may want to use a friction-based clamp to hold a devices such as a mirror in place. An example is shown in Fig. 19. The angle of the mirror, or the phase of the light reflected from it, will affect its performance. In general, we will want to minimize PSTD. Data such as that from Figs. 16 and 17 shows how much we expect the mirrors to move from their intended position as a function of the normal load applied. In general, a friction clamp can be fixed, but the load (or voltage) to fix it in place is significantly larger than suggested by the static coefficient of friction if sliding of less than a few hundred nanometers is required.

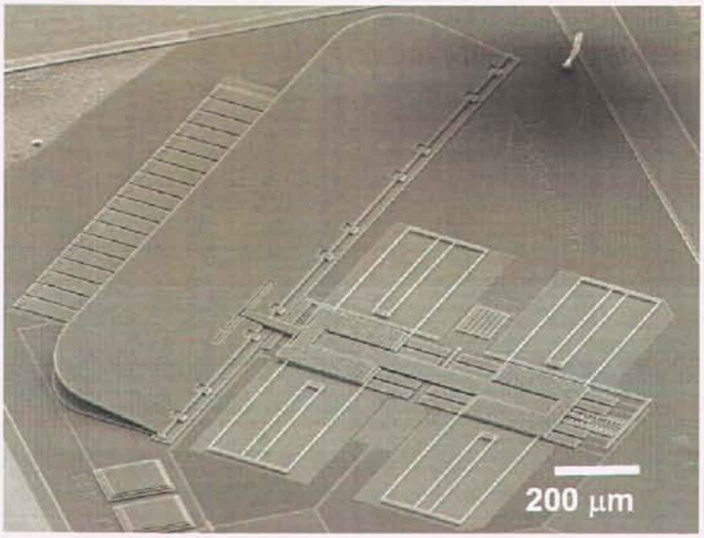

Figure 19 A nanotractor using friction to hold a mirror in place. (Image courtesy of Daryl Dagel, Dept. 1769).

A summary plot of the PSTD data is shown for the various coatings in Fig. 20. PSTD was defined as any device motion before a jump of a minimum size of 100 nm. Of the surfaces intentionally coated , FOTAS has the least PSTD, while OTS has the most. The uncoated surfaces show equal or less PSTD than FOTAS. Hence, although FOTAS, tends to have higher μ_s, both F_A and characteristic PSTD lengths are smaller than the other monolayer coatings. Again, it should be kept in mind that this data is from Lot 247, and splits 1, 4 and 5 have many particles as seen in Fig. 2(b).

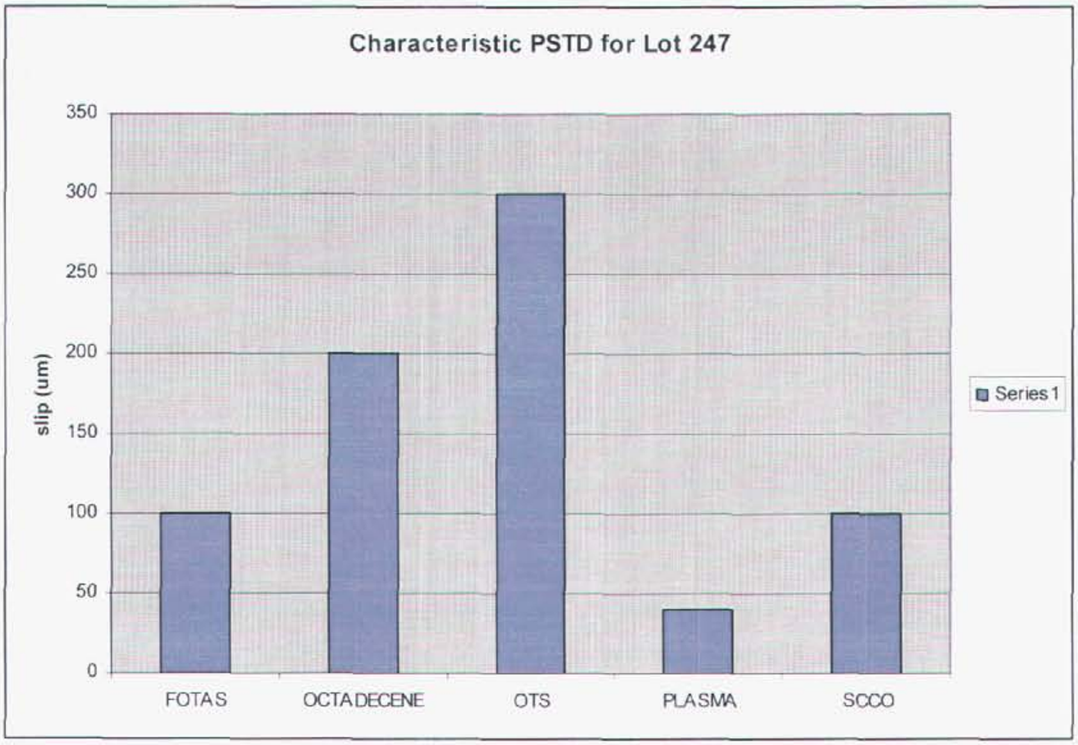

Figure 20 Typical PSTD slip lengths for devices on Lot 247. Slip length is defined as distance traveled between jumps, where a jump is defined as a change in position of 0.1 um.

V.5 TIME DEPENDENCE FOR OTS SLIP

With OTS, the characteristic jump distances are often very small as seen for example in Fig. 13(e). Furthermore, the static and dynamic friction are nearly the same. Therefore, with this coating, it becomes much more difficult to clearly define the friction jumps - the data almost appears continuous. We changed the voltage ramp down procedure to see if, unlike FOTAS, there is a time-dependence of PSTD for this coating, and in fact found that the tangential deflections are not stable with time.

We capture this time dependence through a measurement procedure in which we continue taking data at a specific normal force until the motion of the nanotractor has stopped (as defined by a motion of less than 1 nm over 10 seconds). A comparison of the data under normal test conditions and the modified conditions is shown in Fig. 21. Figure 21 shows the measured time dependence for a particular slip event. We observe motion on the order of 3 μm occurring over about 250 seconds, even though the normal force is held constant. This same measurement applied to FOTAS and octadecene-coated nanotractors showed no time dependence.

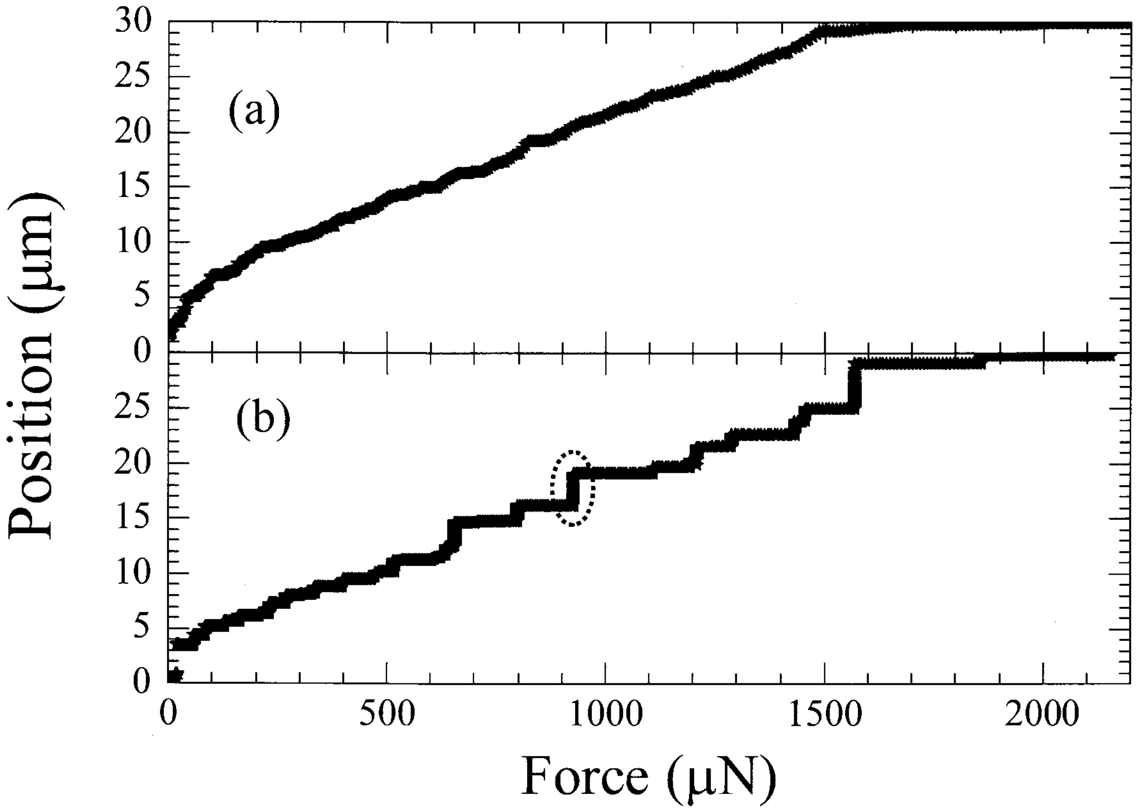

Figure 21 **Panel (a) shows regular friction test with OTS coated nanotractor. Panel (b) shows friction test where normal force is ramped down only after equilibrium position is reached. This data is from Lot 415 (Split 8).**

The experiment here is essentially a stress relaxation experiment and indicates that OTS exhibits a creep-like behavior. Of particular note, in Figure 22 we observe a region where the motion of the nanotractor appears to be slowing (between 100 and 130 seconds). However, at around 135 seconds the nanotractor begins sliding again. This behavior hence appears to be a convolution of the OTS film characteristics and the detailed multi-asperity interactions.

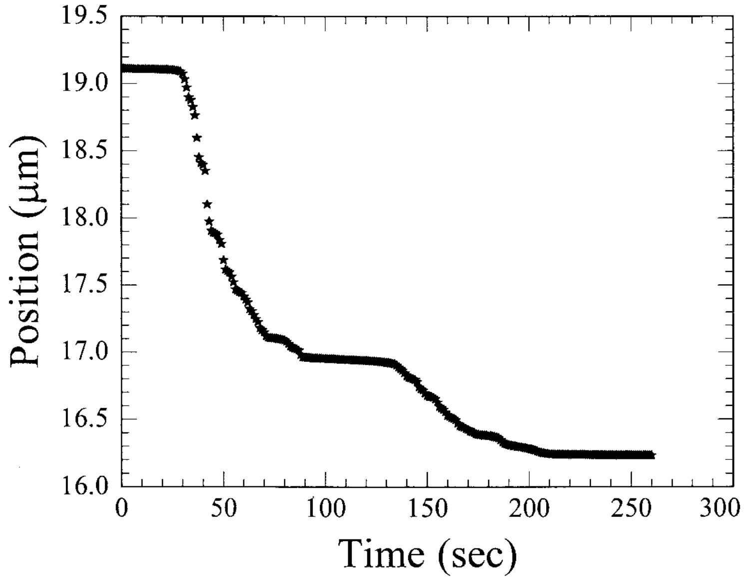

Figure 22 The time dependence from one of the events in figure 20 (as designated by the dotted circle) for an OTS coated nanotractor. In this plot, normal load is held constant.

VI MECHANICS MODEL FOR PSTD

In this section we consider and reject various ideas that could explain PSTD of FOTAS, and then propose and examine a very simple theory that is consistent with our results. Finally, we consider ideas about the creep-like behavior of OTS.

VI. 1 PSTD THEORIES

Numerous theories have been proposed for PSTD-like behavior. At their root is the notion of microslip, which was first described by Mindlin [47]. This theory considers a sphere subject to normal loading and making contact with a flat of diameter $2a$. When tangentially loaded, the elastic compliance of the body can be calculated assuming the interface strength is determined locally by Amontons' First Law, i.e., $\tau_{ys} = \mu\ p$ where p is the local pressure according to Hertz theory. As the tangential load increases, the interface gradually slips locally until the slip zone reaches the center of the contact, which is taken to be the static friction load. The remote tangential deflection is on the order of $0.2a$, as has been confirmed experimentally [48]. The theory has been extended to a Dugdale cohesive zone law [49]. Microslip theories have also been extended to multi-asperity interfaces [8,50]. Although the details change, the tangential deflection at the transition to dynamic friction remains a small fraction of the contact diameter. The slip we measure is ~100 nm for the FOTAS coating. The radius of curvature of the MEMS asperities is typically 100 nm, and under reasonable loads, the contact diameter is ~10 nm. Hence, Mindlin-like microslip theories predict only ~1 nm slip, and cannot explain our PSTD measurements.

Plastic deformation of the asperities would lead to larger slip lengths than suggested by the microslip theories. According to this idea, plastic shear of the asperities would increase the effective contact area. However, when plasticity is introduced into Hertz theory, calculations indicate that contact diameters change by less than 100% for silicon, which is a hard material. Therefore, it is difficult to imagine how this would increase the slip length by a factor of 100. Moreover, the interface is weak due to the monolayer lubricant. This makes it difficult to enhance shear stresses above those from normal stresses only. Finally, the PSTD is quite reproducible from one run to the next. If plastic deformation were important, we would expect the phenomenon to diminish rapidly as the plasticity saturates.

Elastic stretching of the clamps also cannot explain the PSTD. For the maximum tangential force applied, we would expect ~5 nm elastic extension if the clamp were pinned on the trailing end and otherwise free. This is again much less than the measured deflections. Furthermore, the deflections do not depend on the location along the clamp at which they are measured.

Another possibility we considered is that because the friction feet in Lot 247 are curved downward, it might be easy to slide around asperities in a two-dimensional random walk. However, this again seems unlikely because the friction feet in Lot 415 are nominally flat, and therefore have more constraint against this. The fact that we have seen the behavior on multiple lots with different foot shapes and different coatings suggests that this behavior is general and not related to specific contact geometries.

It is also worthwhile to mention that the transition from static to dynamic friction has been the subject of recent experimental study [51]. Direct observations through transparent materials of a rough interface subject to impulse loading indicate that the transition from static to dynamic friction initiates with Rayleigh waves. Unexpectedly, subsonic waves traveling ~1/10th of the sound velocity are required to complete the transition. Once moving, the contact area reduces by ~10%, which lends understanding to the Third Law of friction. Although similar phenomena may be associated with the transition to dynamic friction in the nanotractor interfaces, kinetic energy arguments are not required to simulate the observed stable deflection behavior, as we shall see next.

VI.2 PSTD MECHANICS MODEL

A simple contact model based on geometric interactions was proposed to simulate the quasi-static response of the nanotractor during static friction tests. A representative physical polysilicon surface was chosen from which a direct contact mechanics analysis was performed. The profiles of the contacting surfaces were sampled from an AFM scan of a polysilicon surface. A portion of the polysilicon surface from which the contacting surfaces were sampled is shown in Figure 23. The full scan is 10 μm x 10 μm (1024 x 1024 pixels) with surface roughness of 2.7 nm rms.

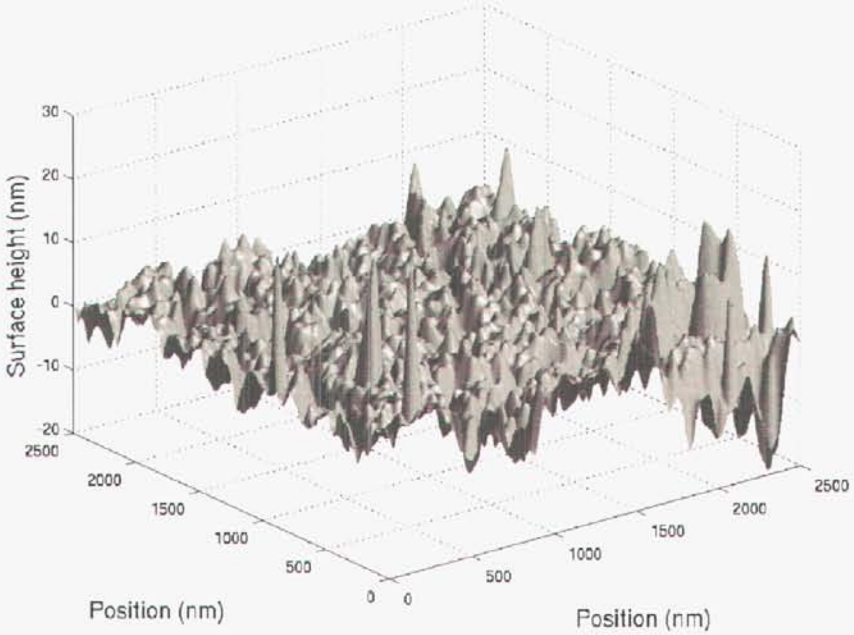

Figure 23. Height profile of the AFM scan from which the contacting nanotractor surfaces were sampled. The image is a 2.5 μm x 2.5 μm sample from a 10 μm x 10 μm scan with 2.7 rms roughness.

The contact mechanics model is a re-creation of the experimental conditions described previously. In addition to the intrinsic assumptions associated with linear elastic analyses, the contact analysis also employed the standard assumptions of Hertzian contact for multiple asperities under silicon-on-silicon contact. The model is quasi-static and therefore cannot capture any of the behavior during the instability and the inertial effects associated with that instability. However, since PSTD occurs during the stable phases of displacement during experiment, a linear elastic representation may accurately reflect the physics.

The model simulation begins by pressing the sliding counterface incrementally (0.01 nm) into the substrate. At each step, local effective interpenetration and radii of curvature are calculated. The counterface is pressed into the substrate until the sum of the local contact forces is equivalent to a predetermined normal force (that of the experiment). Once this force level is achieved, the force that can be resisted in shear can be calculated directly using the current contact area and the assumed junction strength.

$$F_{shear} = \tau A \tag{13}$$

Consistent with the static friction tests, a linear tangential restoring force is applied to the counterface. This non-linear restoring force is developed in the device as it is displaced a distance from its neutral position. The initiation of quasi-static displacement begins by comparing the junction force and the device restoring force. The local conditions are tested to determine whether the counterface moves tangentially or remains in equilibrium. The simulation proceeds in a manner consistent with the experiment until the length of the sampled substrate is traversed.

The algorithm used to look for PSTD are as follows:

<u>Simulation Algorithm:</u>

1) Obtain 2-D linescan of the surface (from real AFM data).
2) Calculate real contact area at a large normal load (Hertz only).
3) Reduce normal load -> contact area reduces
4) When frictional force is surmounted, move clamp forward by an arbitrarily small distance (1 nm used here). Reduce tangential load accordingly.
5) If new position has large enough contact area, then new position is stable. Return to Step (3).
6) If new position is not stable, move clamp forward again by 1 nm. Check if friction force is greater than spring force. If not, continue moving forward. If large enough, new position is stable. Return to Step (3).

A representative simulation result is shown in Figure 24. The figure contains signatures that resemble static friction tests. The simulation features the apparent non-classical response known as PSTD. In particular, we observe slip lengths on the order of 100 nm, as seen in the inset of Fig. 24.

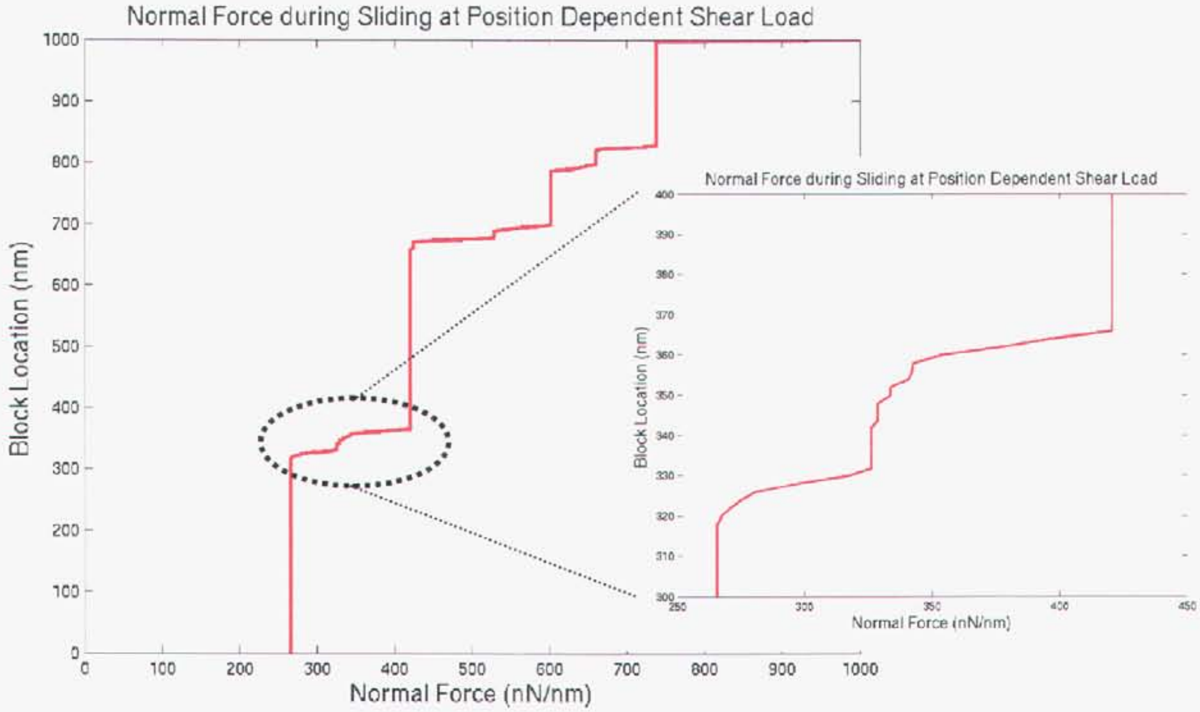

Figure 24. The model simulates PSTD. The inset shows details of the simulated PSTD which have a deflection length scale off the same as order as that seen experimentally

An objection to the analysis leading to Fig. 24 is that the sliding block is only one micron long, much shorter than the actual nanotractor foot, which is 600 μm in length (this was chosen to minimize computation time). To address this issue, Figure 25 features simulations performed to more closely match the number of contacting asperities expected in experiment. In each instance the substrate and counterface profiles were the same. However, the apparent contact area was varied by linking different numbers of the same counterface to move in unison. At the largest apparent contact area, the initial number of contacting asperities was on the order of the number expected during the static friction experiments. The figure shows that the response curve of each simulation was qualitatively similar; however, PSTD events did not occur in each of the simulations. A conclusion to draw from this outcome is that the occurrence of PSTD is a complex function of spatial features coupled with the local contact mechanics. Unfortunately, this appears to render determination of phenomenological parameters difficult if not impossible.

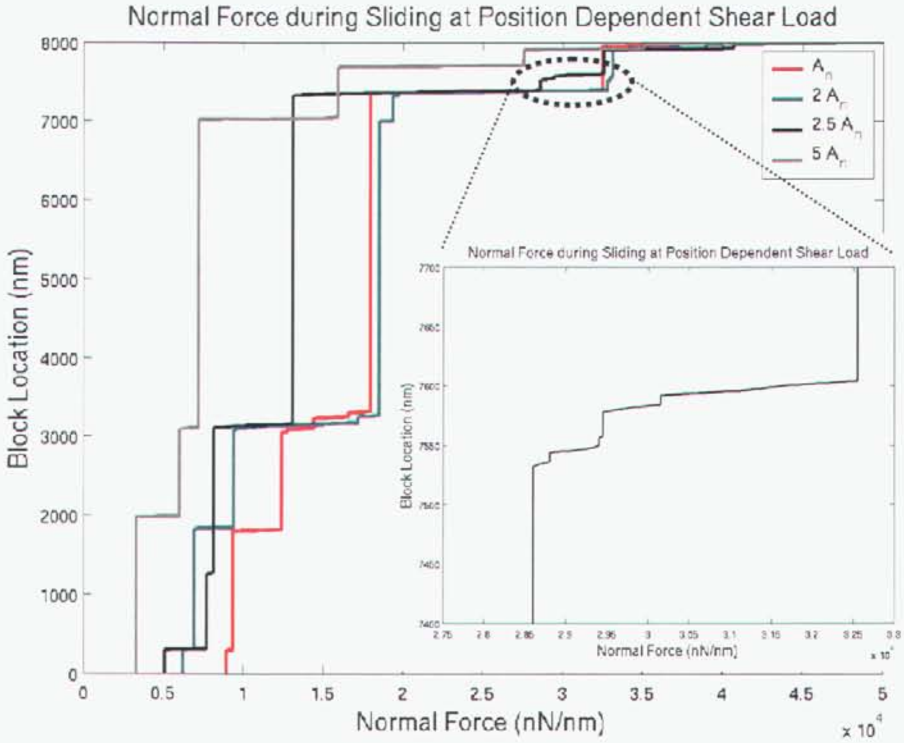

Figure 25. A model simulation in which the effective contact area was increased while applying the same initial normal and tangential forces. The appearance of PSTD in only one of the cases implies a complex dependence of the effect on surface topography and local contact mechanics.

According to this analysis, the phenomenology of the PSTD mechanism cannot be determined *a priori* through independent investigation of the two intimately contacting surfaces. An interrogation of the simulation shown in Figure 25 revealed that during PSTD, the number of contacting asperities remains constant, but perhaps more interestingly, the true contact area also remains essentially constant. This seems to provide further evidence for a randomly occurring event.

VI.3 DISCUSSION OF CREEP IN OTS

The OTS chain displays a strong creep-like effect while octadecene shows a weak effect and neither FOTAS nor the CPD-dried surfaces show evidence of creep. The OTS chain is longer than the FOTAS chain. Also, the local order in OTS is much higher than the FOTAS chain and likely higher than the octadecene chain. We might first consider that polymers also tend to creep. The mechanism for this behavior is that long, tangled molecules tend to straighten out. Given that the OTS molecules are already better organized than the others, this mechanism seems unlikely here.

The static and dynamic friction are very nearly the same for OTS. Because the chains are already relatively well ordered, perhaps their configuration changes little when they come into contact. On the other hand, contacting FOTAS molecules are more likely to reorganize because they are more disordered. With time, this leads to greater interface bonding and hence greater friction. The fact that adhesion is greater for OTS might argue against this idea. However, adhesion may be larger simply because for OTS the monolayer compliance is greater, leading to larger contact areas. We suggest that the creep behavior for OTS emerges because the static and dynamic friction are the same. This makes the friction jumps very small, and in a concerted manner makes it more likely for activated processes to come into play. We will vary temperature in future experiments to determine an activation energy, which we hope will shed more light on this mechanism.

VII. CONCLUSIONS

Monolayer structure has a strong influence on frictional characteristics in MEMS. To make the best choice for a given application, it is important to quantify the effects and evaluate the tradeoffs. Examining the laws of friction, we see that the degree to which they are obeyed depends on the monolayer. In this work, we have investigated the first and third laws, and also have carefully examined the transition from static to dynamic friction. For all three monolayers, there is a deviation from the first law in that $F_A>0$ and further when examined over a wide force range, $F_A=F_A(F_C)$. FOTAS obeys the third law, but OTS appears not to. All three coatings exhibit significant slip prior to the static friction limit in the static friction test, and OTS displays an even more pronounced creep-like effect. From the point of view of the rate and state friction phenomenology, the first two coatings fit into the framework well, but OTS does not.

The experiments so far are compromised in that particles contaminated some of the FOTAS surfaces, as well as the CPD and plasma cleaned surfaces. We will work to obtain more results without these particles so that our interpretations are not affected by this concern.

VIII REFERENCES

[1] D. Dowson, *History of Tribology* (Longman, London and New York, 1979).

[2] G. Amontons, *On the resistance originating in machines (in French)*, Mém. Acad. Roy. A, 206-222 (1699).

[3] C. A. Coulomb, *The theory of simple machines (in French)*, Mem. Math. Phys. Acad. Sci. **10**, 161-331 (1785).

[4] J. T. Desaguliers, *A course of experimental philosophy*, Vol. 1 (London, 1734).

[5] A. R. Burns, J. E. Houston, R. W. Carpick and T. A. Michalske, *Friction and molecular deformation in the molecular regime*, Phys. Rev. Lett. **82** (6), 1181 (1999).

[6] A. D. Corwin and M. P. de Boer, *Effect of adhesion on dynamic and static friction in surface micromachining*, Appl. Phys. Lett. **84** (13), 2451 (2004).

[7] J. Ni and Z. Q. Zhu, *Experimental study of tangential micro deflection of interface of machined surfaces*, J. Manuf. Sci. & Eng. - Trans. ASME **123** (2), 365 (2001).

[8] T. Fujimoto, Kagami J, T. Kawaguchi and T. Hatazawa, *Micro-displacement characteristics under tangential force*, Wear **241**, 136 (2000).

[9] F. Heslot, T. Baumberger, B. Perrin, B. Caroli and C. Caroli, *Creep, stick-slip and dry-friction dynamics: experiments and a heuristic model*, Phys. Rev. E **49** (6), 4973 (1994).

[10] F.-J. Elmer, *Non-linear dynamics of dry friction*, J. Phys. A: Math. Gen. **30**, 6057 (1997).

[11] J. H. Dieterich and B. D. Kilgore, *Direct observations of frictional contacts - new insights for state-dependent properties*, Pure & Appl. Geophys. **143** (1-3), 283 (1994).

[12] P. Berthoud, T. Baumberger, C. G'Sell and J.-M. Hiver, *Physical Analysis of the state- and rate-dependent friction law: static friction*, Phys. Rev. B **59** (22), 14313 (1999).

[13] T. Baumberger, P. Berthoud and C. Caroli, *Physical analysis of the state- and rate-dependent friction law: II. dynamic friction*, Phys. Rev. B **60** (6), 3928 (1999).

[14] J. C. Gu, J. R. Rice, A. L. Ruina and S. T. Tse, *Slip motion and stability of a single degree of freedom elastic system with rate and state dependent friction*, J. Mech. Phys. Sol. **32** (3), 167 (1984).

[15] J. H. Dieterich and B. Kilgore, *Implications of fault constitutive properties for earthquake prediction*, Proc. Natl. Acad. Sci. USA **93**, 3787 (1996).

[16] D. Coker, G. Lykotrafitis, A. Needlman and A. J. Rosakis, *Frictional sliding modes along an interface between identical elastic plates subject to shear impact loading*, J. Mech. Phys. Sol. **53** (4), 884 (2005).

[17] J. K. Morgan, *Particle dynamics simulations of rate- and state-dependent frictional sliding of granular fault gouge*, Pure & Appl. Geophys. **161** (9-10), 1877 (2004).

[18] J. J. Sniegowski and M. P. de Boer, *IC-compatible polysilicon surface micromachining*, Annu. Rev. Mater. Sci. **30**, 297 (2000).

[19] K. H. L. Chau and R.E. Sulouff, *Technology for the high-volume manufacturing of integrated surface-micromachined accelerometer products*, Microelectronics Journal **29** (9), 579 (1998).

[20] J. Schuster and D. Monk, *Micromachined pressure sensors pave way for new process solutions.*, 43-4, 47, 49-50 **73** (11), 43 (2000).

[21] D. M. Tanner and M.T. Dugger, *Wear mechanisms in a reliability methodology*, Proc. of the SPIE Vol. 4980, 2003), pp. 22-40.

[22] D. L. Luck, M. P. de Boer, W. R. Ashurst and M. S. Baker, *Evidence for pre-sliding tangential deflections in MEMS friction*, Transducers 2003, Boston 2003), pp. 404-407.

[23] A. D. Corwin, M. D. Street, R. W. Carpick, W. R. Ashurst and M. P. de Boer, *Presliding tangential deflections can govern the friction of MEMS devices.*, Proc. ASME/STLE Joint International Tribology Conf., Long Beach 2004).

[24] M. P. de Boer, D. L. Luck, W. R. Ashurst, A. D. Corwin, J. A. Walraven and J. M. Redmond, *High-performance surface-micromachined inchworm actuator*, J. Microelectromech. Syst. **13** (1), 63 (2004).

[25] W. C. Tang, T. C. H. Nguyen and R. T. Howe, *Laterally driven polysilicon resonant microstructures*, Sensors and Actuators A **20** (1-2), 25 (1989).

[26] S.L. Miller, M.S. Rodgers, G. La Vigne, J. J. Sniegowski, P. J. Clews, D.M. Tanner and K.A. Peterson, *Failure modes in surface micromachined microelectromechanical actuation systems*, Microelectronics Reliability **39** (8), 1229 (1999).

[27] C. H. Mastrangelo and C. H. Hsu, *Mechanical stability and adhesion of microstructures under capillary forces-part I: basic theory*, J. Microelectromech. Syst. **2** (1), 33 (1993).

[28] C. H. Mastrangelo and C. H. Hsu, *Mechanical stability and adhesion of microstructures under capillary forces-part II: experiments*, J. Microelectromech. Syst. **2** (1), 44 (1993).

[29] G. T. Mulhern, D. S. Soane and R. T. Howe, *Supercritical carbon dioxide drying of microstructures*, Proc. 7th Int. Conf. Solid-State Sensors and Actuators, Transducers '93, Yokohama, Japan (June 7-10 1993), pp. 296-299.

[30] M. G. Hankins, P. J. Resnick, P. J. Clews, T. M. Mayer, D. R. Wheeler, D. M. Tanner and R. A. Plass, *Vapor deposition of amino-functionalized self-assembled monolayers on MEMS*, Proceedings of the SPIE, Vol. 4980, edited by R. Ramesham and D. M. Tanner, San Francisco 2003), pp. 238-247.

[31] T. M. Mayer, M. P. de Boer, N. D. Shinn, P. J. Clews and T. A. Michalske, *Chemical vapor deposition of fluoroalkylsilane monolayer films for adhesion control in microelectromechanical systems*, Journal of Vacuum Science and Technology B **18** (5), 2433 (2000).

[32] U. Srinivasan, M. R. Houston, R. T. Howe and R. Maboudian, *Alkyltrichlorosilane-based self-assembled monolayer films for stiction reduction in silicon micromachines*, J. Microelectromech. Syst. **7** (2), 252 (1998).

[33] W. R. Ashurst, C. Yau, C. Carraro, C. Lee, R. T. Howe and R. Maboudian, *Alkene based monolayer films as anti-stiction coatings for polysilicon MEMS*, Sensors and Actuators A **9** (3), 239 (2001).

[34] F. Schreiber, *Structure and growth of self-assembling monolayers*, Prog. Surf. Sci. **65**, 151 (2000).

[35] J. Israelachvili, *Intermolecular and Surface Forces* (Academic Press, New York, 1992).

[36] M. D. Porter, T. B. Bright, D. L. Allara and C. E. D. Chidsey, *Spontaneously organized molecular assemblies. 4. Structural characterization of n-alkyl thiol monolayers on gold by optical ellipsometry, infrared spectroscopy and electrochemistry*, J. Am. Chem. Soc. **109**, 3559 (1987).

[37] C. Carraro, O. W. Yauw, M. M. Sung and R. Maboudian, *Observation of three growth mechanisms in self-assembled monolayers*, J. Phys. Chem. B **102** (23), 4441 (1998).

[38] R. W. Carpick and M. Salmeron, *Scratching the surface: Fundamental investigations of tribology with atomic force microscopy*, Chemical Reviews **97** (4), 1163 (1997).

[39] M. J. Stevens, *Thoughts on the structure of alkylsilane monolayers*, Langmuir **15** (8), 2773 (1999).

[40] I.M. Tidswell, T.A. Rabedeau, P.S. Pershan, S.D. Kosowsky, J.P. Folkers and G.M. Whitesides, *X-ray grazing incidence diffraction from alkylsiloxane monolayers on silicon wafers*, J. Chem. Phys. **95**, 2854 (1991).
[41] B. C. Bunker, R. W. Carpick, R. Assink, M. L. Thomas, M. G. Hankins, J. A. Voigt, D. L. Sipola, M. P. de Boer and G. L. Gulley, *The impact of solution agglomeration on the deposition of self-assembled monolayers*, Langmuir **16**, 7742 (2000).
[42] J. G. Kushmerick, M. G Hankins, M. P. de Boer, P. J. Clews, R. W. Carpick and B. C. Bunker, *The influence of coating structure on micromachine stiction*, Tribol. Lett. **10** (1-2), 103 (2001).
[43] J. A. Greenwood and J. B. P. Williamson, *Contact of nominally flat surfaces*, Proc. Roy. Soc. Lond. A. **295**, 300 (1966).
[44] J. A. Greenwood and J. H. Tripp, *The contact of two nominally flat rough surfaces*, Proc. Instn. Mech. Engrs. **185**, 625 (1970-71).
[45] D. Maugis, *On the contact and adhesion of rough surfaces*, J. Adh. Sc. Tech. **10** (2), 161 (1996).
[46] N. R. Tas, C. Gui and M. Elwenspoek, *Static friction in elastic adhesion contacts in MEMS*, J. Adh. Sc. Tech. **17** (4), 547 (2003).
[47] R. D. Mindlin, *Compliance of elastic bodies in contact*, J. Appl. Mech. **16** (3), 259 (1949).
[48] J.S. Courtney-Pratt and E. Eisner, *The effect of tangential force on the contact of metallic bodies*, Proc. Roy. Soc. Lond. A. **238**, 529 (1957).
[49] K. L. Johnson, *Adhesion and friction between a smooth elastic spherical asperity and a plane surface*, Proc. Roy. Soc. Lond. A. **453** (1956), 163 (1997).
[50] P. Berthoud and T. Baumberger, *Shear stiffness of a solid-solid multicontact interface*, Proc. Roy. Soc. Lond. A. **454**, 1615 (1997).
[51] S. M. Rubinstein, G. Cohen and J. Fineberg, *Detachment fronts and the onset of dynamic friction*, Nature **430** (7003), 1005 (2004).

Distribution

2	MS1310	Maarten P. de Boer, 1769
1	MS1310	Alex D. Corwin, 1749
1		Mark D. Street
1		Robert W. Carpick
1	MS9051	William R. Ashurst
1	MS0847	Michael J. Starr
1	MS1080	David R. Sandison, 1769
1	MS0893	Dave Reedy, 1523
1	MS0834	Joel Lash, 1514
1	MS0123	LDRD Office, Donna Chavez, 01011
2	MS0899	Technical Library, 4536
2	MS9018	Central Technology Files, 8945-1